Differential Photoproduction Cross Sections of the $\Sigma^0(1385)$, $\Lambda(1405)$, and $\Lambda(1520)$

K. Moriya,[1, *] R.A. Schumacher,[1] K.P. Adhikari,[29] D. Adikaram,[29] M. Aghasyan,[18] M.J. Amaryan,[29]
M.D. Anderson,[38] S. Anefalos Pereira,[18] H. Avakian,[35] J. Ball,[7] N.A. Baltzell,[2, 34] M. Battaglieri,[19]
V. Batourine,[35, 24] I. Bedlinskiy,[22] M. Bellis,[1, †] R. P. Bennett,[29] A.S. Biselli,[11, 1] J. Bono,[12] S. Boiarinov,[35]
W.J. Briscoe,[15] W.K. Brooks,[37, 35] V.D. Burkert,[35] D.S. Carman,[35] A. Celentano,[19] S. Chandavar,[28] P. Collins,[6]
M. Contalbrigo,[17] O. Cortes,[16] V. Crede,[13] A. D'Angelo,[20, 32] N. Dashyan,[41] R. De Vita,[19] E. De Sanctis,[18]
A. Deur,[35] B. Dey,[1] C. Djalali,[34] D. Doughty,[8, 35] M. Dugger,[3] R. Dupre,[21] H. Egiyan,[35] L. El Fassi,[2] P. Eugenio,[13]
G. Fedotov,[34, 33] S. Fegan,[19] R. Fersch,[8] J.A. Fleming,[10] N. Gevorgyan,[41] G.P. Gilfoyle,[31] K.L. Giovanetti,[23]
F.X. Girod,[35, 7] J.T. Goetz,[28] W. Gohn,[9] E. Golovatch,[33] R.W. Gothe,[34] K.A. Griffioen,[40] M. Guidal,[21]
N. Guler,[29, ‡] L. Guo,[12, 35] H. Hakobyan,[37, 41] C. Hanretty,[39, 13] D. Heddle,[8, 35] K. Hicks,[28] D. Ho,[1] M. Holtrop,[26]
Y. Ilieva,[34, 15] D.G. Ireland,[38] B.S. Ishkhanov,[33] E.L. Isupov,[33] H.S. Jo,[21] K. Joo,[9] D. Keller,[39] M. Khandaker,[27]
A. Klein,[29] F.J. Klein,[6] S. Koirala,[29] A. Kubarovsky,[9, 33] V. Kubarovsky,[35, 30] S.V. Kuleshov,[37, 22] S. Lewis,[38]
K. Livingston,[38] H.Y. Lu,[1, 34] I.J.D. MacGregor,[38] D. Martinez,[16] M. Mayer,[29] M. McCracken,[1] B. McKinnon,[38]
M.D. Mestayer,[35] C.A. Meyer,[1] T. Mineeva,[9] M. Mirazita,[18] V. Mokeev,[35, 33] R.A. Montgomery,[38] H. Moutarde,[7]
E. Munevar,[35, 15] C. Munoz Camacho,[21] P. Nadel-Turonski,[35] R. Nasseripour,[23, 34] C.S. Nepali,[29] S. Niccolai,[21]
G. Niculescu,[23] I. Niculescu,[23] M. Osipenko,[19] A.I. Ostrovidov,[13] L.L. Pappalardo,[17] R. Paremuzyan,[21] K. Park,[35, 24]
S. Park,[13] E. Pasyuk,[35, 3] E. Phelps,[34] J.J. Phillips,[38] S. Pisano,[18] O. Pogorelko,[22] S. Pozdniakov,[22] J.W. Price,[4]
S. Procureur,[7] D. Protopopescu,[38] A.J.R. Puckett,[35] B.A. Raue,[12, 35] D. Rimal,[12] M. Ripani,[19] B.G. Ritchie,[3]
G. Rosner,[38] P. Rossi,[18] F. Sabatié,[7] M.S. Saini,[13] C. Salgado,[27] D. Schott,[15] E. Seder,[9] H. Seraydaryan,[29]
Y.G. Sharabian,[35] G.D. Smith,[38] D.I. Sober,[6] D. Sokhan,[38] S. Stepanyan,[35] P. Stoler,[30] S. Strauch,[34, 15]
M. Taiuti,[14] W. Tang,[28] C.E. Taylor,[16] S. Taylor,[35] Y. Tian,[34] S. Tkachenko,[39] M. Ungaro,[35, 9, 30]
B .Vernarsky,[1] M.F. Vineyard,[36] H. Voskanyan,[41] E. Voutier,[25] N.K. Walford,[6] D.P. Watts,[10] L.B. Weinstein,[29]
M. Williams,[1] M.H. Wood,[5, 34] N. Zachariou,[34] L. Zana,[26] J. Zhang,[35] Z.W. Zhao,[39] and I. Zonta[20]

(The CLAS Collaboration)

[1] *Carnegie Mellon University, Pittsburgh, Pennsylvania 15213*
[2] *Argonne National Laboratory, Argonne, Illinois 60439*
[3] *Arizona State University, Tempe, Arizona 85287-1504*
[4] *California State University, Dominguez Hills, Carson, CA 90747*
[5] *Canisius College, Buffalo, NY*
[6] *Catholic University of America, Washington, D.C. 20064*
[7] *CEA, Centre de Saclay, Irfu/Service de Physique Nucléaire, 91191 Gif-sur-Yvette, France*
[8] *Christopher Newport University, Newport News, Virginia 23606*
[9] *University of Connecticut, Storrs, Connecticut 06269*
[10] *Edinburgh University, Edinburgh EH9 3JZ, United Kingdom*
[11] *Fairfield University, Fairfield CT 06824*
[12] *Florida International University, Miami, Florida 33199*
[13] *Florida State University, Tallahassee, Florida 32306*
[14] *Università di Genova, 16146 Genova, Italy*
[15] *The George Washington University, Washington, DC 20052*
[16] *Idaho State University, Pocatello, Idaho 83209*
[17] *INFN, Sezione di Ferrara, 44100 Ferrara, Italy*
[18] *INFN, Laboratori Nazionali di Frascati, 00044 Frascati, Italy*
[19] *INFN, Sezione di Genova, 16146 Genova, Italy*
[20] *INFN, Sezione di Roma Tor Vergata, 00133 Rome, Italy*
[21] *Institut de Physique Nucléaire ORSAY, Orsay, France*
[22] *Institute of Theoretical and Experimental Physics, Moscow, 117259, Russia*
[23] *James Madison University, Harrisonburg, Virginia 22807*
[24] *Kyungpook National University, Daegu 702-701, Republic of Korea*
[25] *LPSC, Universite Joseph Fourier, CNRS/IN2P3, INPG, Grenoble, France*
[26] *University of New Hampshire, Durham, New Hampshire 03824-3568*
[27] *Norfolk State University, Norfolk, Virginia 23504*
[28] *Ohio University, Athens, Ohio 45701*
[29] *Old Dominion University, Norfolk, Virginia 23529*
[30] *Rensselaer Polytechnic Institute, Troy, New York 12180-3590*
[31] *University of Richmond, Richmond, Virginia 23173*
[32] *Universita' di Roma Tor Vergata, 00133 Roma Italy*
[33] *Skobeltsyn Nuclear Physics Institute, 119899 Moscow, Russia*
[34] *University of South Carolina, Columbia, South Carolina 29208*

[35] *Thomas Jefferson National Accelerator Facility, Newport News, Virginia 23606*
[36] *Union College, Schenectady, NY 12308*
[37] *Universidad Técnica Federico Santa María, Casilla 110-V Valparaíso, Chile*
[38] *University of Glasgow, Glasgow G12 8QQ, United Kingdom*
[39] *University of Virginia, Charlottesville, Virginia 22901*
[40] *College of William and Mary, Williamsburg, Virginia 23187-8795*
[41] *Yerevan Physics Institute, 375036 Yerevan, Armenia*

We report the exclusive photoproduction cross sections for the $\Sigma^0(1385)$, $\Lambda(1405)$, and $\Lambda(1520)$ in the reactions $\gamma + p \to K^+ + Y^*$ using the CLAS detector for energies from near the respective production thresholds up to a center-of-mass energy W of 2.85 GeV. The differential cross sections are integrated to give the total exclusive cross sections for each hyperon. Comparisons are made to current theoretical models based on the effective Lagrangian approach and fitted to previous data. The accuracy of these models is seen to vary widely. The cross sections for the $\Lambda(1405)$ region are strikingly different for the $\Sigma^+\pi^-$, $\Sigma^0\pi^0$, and $\Sigma^-\pi^+$ decay channels, indicating the effect of isospin interference, especially at W values close to the threshold.

PACS numbers: 13.30.Eg 13.40.-f 13.60.Rj 14.20.Gk

I. INTRODUCTION

The $\Lambda(1405)$ ($J^P = 1/2^-$), situated just below the $N\bar{K}$ threshold, has been an enigmatic state in the spectrum of strange baryons for decades. The differential photoproduction cross sections should provide information needed to identify the dynamics that play a significant role in the formation of the $\Lambda(1405)$, and lead to a deeper understanding of any other structures that populate this mass region. The $\Lambda(1405)$ sits between two other well-known hyperons, the $\Sigma^0(1385)$ ($J^P = 3/2^+$) and the $\Lambda(1520)$ ($J^P = 3/2^-$). Also for these states, photoproduction data have been scarce, and comparison of the three hyperons was not practical until now.

The CLAS measurements reported here are the first to have been made for all three excited hyperon species at the same time with the same apparatus and within the same analysis. A critical comparison of the cross sections for the combined set of hyperons, including the ground states, may yield further insight into their structures. In particular, since the $\Lambda(1405)$ does not fit quantitatively into quark model estimations of its mass [1, 2], and since it has always been thought to be strongly influenced by the nearby $N\bar{K}$ and $\Sigma\pi$ thresholds [3, 4], one might expect differences in the mechanism of its production in comparison to the more typical hyperons.

The outline of this paper is as follows. Section II briefly describes several previous hyperon photoproduction experiments, together with several theoretical models that have been proposed. Section III outlines the setup of the experiment and the steps taken toward cross section extractions. Subsection III A discusses the yield extraction for the $\Sigma^0(1385)$ via the $\Lambda\pi$ decay mode and Subsection III B discusses the yields of the $\Lambda(1405)$ and $\Lambda(1520)$

via the three different $\Sigma\pi$ decay modes. Subsection III C then discusses the acceptance calculations computed using a Monte Carlo (MC) method, and the photon beam flux normalization. The systematic uncertainties of the cross section results will be discussed in Subsection III D. Section IV shows the results for each hyperon individually, and then compares the hyperons to each other. We recapitulate the main results in Sec. V.

II. PAST EXPERIMENTS AND CURRENT THEORY

For photoproduction of the $\Sigma^0(1385)$ on the proton there are total cross section measurements from bubble chamber work by the ABBHHM group [5, 6] and by the CEA group [7]. Preliminary results from CLAS have been presented [8], but the present analysis is independent of that study, albeit using the same raw data set. In all these measurements the hyperon was reconstructed through its dominant decay to $\Lambda\pi^0$. Alternatively, the LEPS Collaboration measured $\gamma n \to K^+\Sigma^-(1385)$ using a deuteron target and detected only the K^+ and the π^- from the hyperon decay to $\Lambda\pi^-$ [9]. The LEPS result showed a flat angular distribution for $\cos\theta_{K^+}^{\text{c.m.}} > 0.6$ and an energy dependence that rose from threshold to a wide peak near $W = 1.8$ GeV. That result was compared with an effective Lagrangian model of Oh *et al.* [10] in which the dominant contribution came from t-channel K exchange and little from K^*. Agreement was at best fair, both for the cross section and for the beam asymmetry. One may expect comparable cross sections in the reaction $\gamma p \to K^+\Sigma^0(1385)$, as will be discussed. We will compare our results for this channel with the same model calculation in Sec. IV A.

For photoproduction of the $\Lambda(1520)$ there are previous experimental data from Boyarski *et al.* (SLAC) [11] at $E_\gamma = 11$ GeV and Barber *et al.* (LAMP2, Daresbury) [12] at $E_\gamma = 2.8 - 4.8$ GeV. In more recent times, the LEPS Collaboration has looked at photoproduction

of this hyperon in the energy region $1.9 < E_\gamma < 2.8$ GeV using a forward-angle spectrometer [13, 14]. They showed that the cross section is forward peaked, and that this behavior is more consistent with a model dominated by a gauge-invariance-preserving contact term [15, 16], and less consistent with models dominated by $t-$channel vector meson K^* exchange [17, 18]. However, the K^* exchange models are more consistent with the results at higher photon energies (Ref. [12]). The beam asymmetry for the $\Lambda(1520)$ was found to be small, much smaller than for the ground state Λ, supporting the contact-term model that found K^* exchange is not important in the threshold region. Furthermore, it was found that the energy dependence of the forward-angle cross section rises from threshold to a maximum near $W = 2.15$ GeV, followed by a decline. It was suggested that this could be an effect of an N^* intermediate resonance at 2.11 GeV [16]. The results in the present paper cover a broader kinematic range than previous data, and will be compared to the approach in Ref. [16] and also Ref. [19] in Sec. IV.

Additional $\Lambda(1520)$ photoproduction data close to threshold were published recently by SAPHIR [20], to be discussed later. Pioneering measurements at Cornell [21] and CEA [22] will not be discussed. There is also a $\Lambda(1520)$ electroproduction result from CLAS [23] at $Q^2 > 0.9$ GeV/c^2 that we will not discuss here.

For photoproduction of the $\Lambda(1405)$ there was very little information up to now. The LEPS Collaboration produced the only significant measurement so far [24]. They estimated that the differential cross section for $0.8 < \cos\theta_{K^+}^{c.m.} < 1.0$ and $1.5 < E_\gamma < 2.0$ GeV is about 0.4 μb (no error estimate given, but we suppose it to be $\sim 50\%$). They also reported a steep decrease in $\Lambda(1405)$ production versus $\Sigma^0(1385)$ production in the higher energy range $2.0 < E_\gamma < 2.4$ GeV. They speculated that this might be a hint of strong dynamical differences in the production mechanisms. We will consider these findings in Sec. IV C.

Considering recent theoretical approaches, the photoproduction cross section of the $\Sigma^0(1385)$ has been studied in an effective Lagrangian model of Oh et $al.$ [10]. They pointed out that since the cross section for this excited hyperon is comparable in size to those of the ground state Λ and Σ^0, it also may serve as a hunting ground for high-mass non-strange resonances that may couple to it. The calculation was evaluated at tree-level, with single-channel Born and resonance contributions using empirically obtained couplings. A set of four high mass Δ and N^* resonances was found to contribute to the total cross section for the reaction in the threshold region. However, only a preliminary CLAS total cross section result [8] was available to fit, and the resonances played a secondary role in matching the data. The contact interaction used to preserve gauge invariance was dominant. Thus, the present paper that shows differential cross sections as well as the integrated total cross section should help clarify the theoretical modeling of this reaction, including any resonant content.

The photoproduction cross section of the $\Lambda(1520)$ has been studied theoretically by Nam et $al.$ [15]. In an effective Lagrangian approach, using Born terms and a Rarita-Schwinger formalism for inclusion of the spin-3/2 $\Lambda(1520)$, they tested various model assumptions against scant previous data [12] for the total cross section and the t-dependence at $E_\gamma = 3.8$ GeV. They found that the total cross section near threshold was mainly determined by the contact interaction included in order to preserve gauge invariance in the presence of hadronic form factors. They found only minor sensitivity, for photon energies below 3 GeV, to the anomalous magnetic moment of the hyperon, κ_{Λ^*}, and the coupling constant $g_{K^*N\Lambda^*}$. No N^* (s-channel) resonances were found to be necessary to qualitatively reproduce the cross sections. In a subsequent paper [16] the effect of Reggeizing the $t-$channel exchanges was studied. At CLAS energies (i.e. for $E_\gamma < 3.7$ GeV) this effect was found to be negligible.

In another effective Lagrangian approach model for the $\Lambda(1520)$ cross section, He and Chen studied systematically the inclusion or exclusion of several higher-mass Constituent Quark Model (CQM) nucleon resonances [19]. Their approach was to fit the differential cross sections from LEPS and also the higher energy t-dependence from SLAC. They concluded that the contact term is the dominant contribution to the cross section at all energies. Also, both K and K^* exchanges play a significant role, though the K^* only at the higher SLAC energies. They found significant resonance contribution only from the two-star $N(2080)D_{13}$, and a possible hint that a CQM D_{15} resonance at nearly the same mass could be needed. We note in passing that the $N(2080)D_{13}$ is a state that is important in photoproduction of the ground-state $\Lambda(1116)$ [25]. (Also note that the most recent Particle Data Group (PDG) [26] evaluation of the $N^*3/2^-D_{13}$ partial wave splits this state into two: one at 1875 MeV and one at 2120 MeV.) Their affirmative conclusion about the need for these resonances is in disagreement with the previous work by Nam et $al.$ cited in Ref. [14], and their quantitative agreement with the $\Lambda(1520)$ differential cross section and with the beam asymmetry were not good. We can expect that the more complete angular distributions presented below will be useful in refining these models.

The photoproduction cross section of the $\Lambda(1405)$ has been studied theoretically by Nam et $al.$ [27] within the framework of the same model as discussed above for the $\Lambda(1520)$. Within their effective Lagrangian approach there is a mass cutoff in the electromagnetic form factor for the $\gamma\Lambda^*\Lambda^*$ vertex. By varying this cutoff they hoped to be sensitive to a size effect related to the spatial structure of the $\Lambda(1405)$. However, this u-channel effect turned out to be too small in relation to other theoretical ambiguities to give useful sensitivity. They used chiral unitary model results to estimate $g_{KN\Lambda^*}$, but left $g_{K^*N\Lambda^*}$ as a free parameter. By comparing to the very limited experimental data [24], they concluded that the $\Lambda(1405)$ is produced dominantly by the s-channel Born

contribution, without resonant intermediate states, and not by meson exchange in the t-channel. In an older model, by Williams, Ji and Cotanch [28], emphasis was placed on constraints from crossing symmetry and duality, but gauge invariance was not enforced. The K^* exchange diagram was omitted, and the $\Lambda(1405)$ appeared via resonance in the u-channel. After satisfactory fits were made to photoproduction data for the ground state Λ and Σ^0, a prediction for the threshold cross section of the $\Lambda(1405)$ was made. These two model cross sections will be compared with our results later in Sec. IV C.

Photoproduction of the $\Lambda(1405)$ has also been studied by Nacher *et al.* [29] in the context of examining the $\Sigma\pi$ line shapes. The study used an energy- and angle-independent Weinberg-Tomozawa contact interaction, implying a featureless differential cross section. So while that study was crucial to our previous work in Ref. [30], it is not relevant for the current work of examining the cross sections.

III. EXPERIMENTAL SETUP AND DATA ANALYSIS

The data for this experiment were obtained with the CLAS detector, located in Hall B at the Thomas Jefferson National Accelerator Facility, during May and June of 2004. The run, known as g11a, used a 40-cm unpolarized liquid hydrogen target and an incoming unpolarized real photon beam. Bremsstrahlung photons were created via the CEBAF accelerator electron beam and a thin gold foil radiator, with an endpoint energy of 4.019 GeV. Electrons that radiated a photon were detected with the CLAS tagger [31] to obtain energy and timing information over the range from 20% to 95% of the endpoint energy. Discussion of the CLAS apparatus can be found in Ref. [32]. All aspects of the data collection and initial data handling were discussed in our previous paper [30] that focused on the invariant mass distributions or "line shapes" of the $\Lambda(1405)$. The same analysis extracted the cross sections presented here. Here we review and discuss the important steps related to obtaining the cross sections.

The exclusive channels were reconstruction from the detected K^+ and all but one of the hyperon decay products. A one-constraint kinematic fit to the missing particle was used to select each of the channels; for the decays $\Lambda(1405)/\Lambda(1520) \to \Sigma^0\pi^0$ both a photon and a π^0 were missing, so a simpler missing-mass selection was used instead. The hyperon yields for a given decay channel were obtained in each photon energy and kaon angle bin using an incoherent fit of MC simulations of signal and background channels. The energy bins in center-of-mass energy W were 100 MeV wide. The angle bins in the kaon angle $\cos\theta_{K^+}^{\text{c.m.}}$ were again in the center-of-mass system. In all cases, the fits to each energy and angle bin were treated independently. We next give some examples to illustrate this process.

A. Yields for $\Sigma^0(1385)$

For photoproduction of the $\Sigma^0(1385)$, the cross section was reconstructed from the dominant decay mode to $\Lambda\pi^0$ (B.R. 87.0%), where a kinematic fit to the undetected π^0 was used to optimize the measurements of the energy and momentum of the detected particles. Figure 1 shows two typical sample bins in center-of-mass energy bins that are 100 MeV wide and span a range of 0.1 in $\cos\theta_{K^+}^{\text{c.m.}}$. A full MC simulation of the $K^+\Sigma^0(1385)$ signal reaction was done to create realistic templates which could be fitted to the data. Similarly, the dominant $K^{*+}\Lambda$ background channel was simulated. As discussed in our previous paper [30], the line shape function for the $\Sigma^0(1385)$ was most realistically modeled using a non-relativistic Breit-Wigner form. This fit the data best in all energy and angle bins. The $\Sigma^0(1385)$ yield was taken to be the integrated fitted counts in the template line shape.

In some bins in W there was kinematic overlap of the signal hyperon and the background $K^{*+}\Lambda$ events. Tests showed that there was no discernible coherent interference between the signal and background channels. That is, the cross section results did not change even when a drastic ($\pm 1\Gamma$ or ~ 100 MeV) cut was made to reject events in the kinematic overlap region that contained most of the $K^{*+}\Lambda$ events.

B. Yields for $\Lambda(1405)$ and $\Lambda(1520)$

For photoproduction of the $\Lambda(1405)$ and the $\Lambda(1520)$, the cross sections were determined using the $\Sigma\pi$ decay mode (B.R 100% and 42%, respectively). How this was done is illustrated in Fig. 2. Again, MC simulations were used to realistically model the distribution of events from each of the signal reactions. In the case of the $\Lambda(1520)$ the template shape was a relativistic Breit-Wigner using PDG parameters and processed through the CLAS simulation. The $\Lambda(1405)$ line shape was determined using an iterated MC method since it did not conform to a simple Breit-Wigner shape. The figure shows the initial and the final iteration of the sample fit. The final iteration matches the data much better in the $\Lambda(1405)$ region. The fit also included three background processes. The first was photoproduction of $K^+\Sigma^0(1385)$, which has a known small branching fraction to $\Sigma\pi$. Its strength therefore was not allowed to float in the fit, since the dominant $\Lambda\pi^0$ decay mode determines its size in the $\Sigma\pi$ decay modes, after being corrected by the ratio of known branching fractions and acceptance in each channel. The second backgrounds were the $K^{*0}\Sigma^+$ channels that appeared as a broad distribution in the example shown. Finally there was photoproduction of a higher-mass Y^* centered around 1670 MeV/c^2, which was modeled with a simple Breit-Wigner line shape and not with the full MC simulation, as can be discerned from the smooth curve in Fig. 2.

The important difference between the results for the

(a) $W = 2.1$ GeV, $\cos\theta_{K^+}^{\text{c.m.}} = 0.85$

(b) $W = 2.6$ GeV, $\cos\theta_{K^+}^{\text{c.m.}} = 0.65$
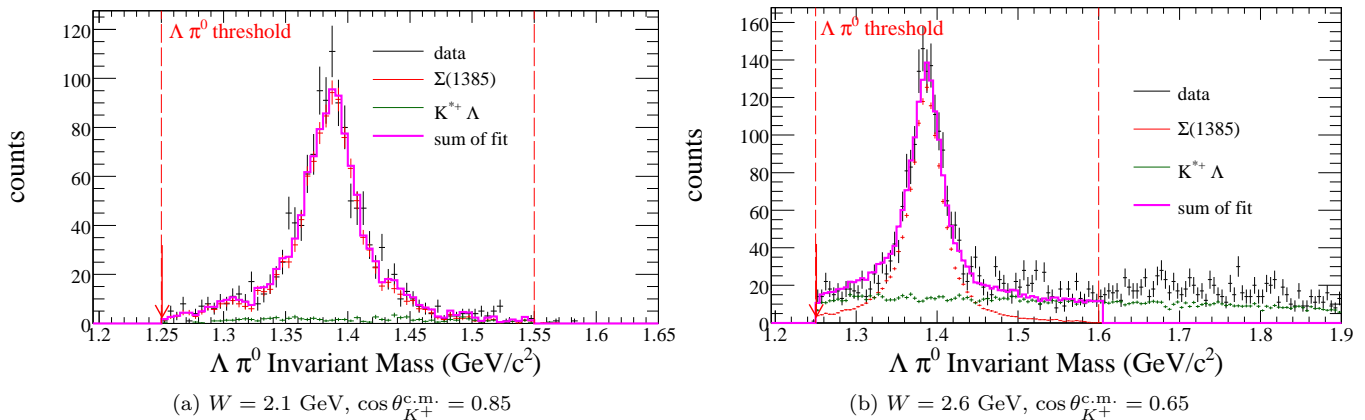
FIG. 1. (Color online) Sample fit results of the strong final state of $K^+\Lambda\pi^0$. The events are plotted versus the missing mass from the K^+, which is equivalent to the invariant mass of the $\Lambda\pi^0$ system. The data are shown by the black crosses, while the $\Sigma^0(1385)$ signal MC and the $K^{*+}\Lambda$ background are shown by the red crosses and green circles, respectively. The sum of the MC templates is shown by the solid magenta line.


(a)

(b)
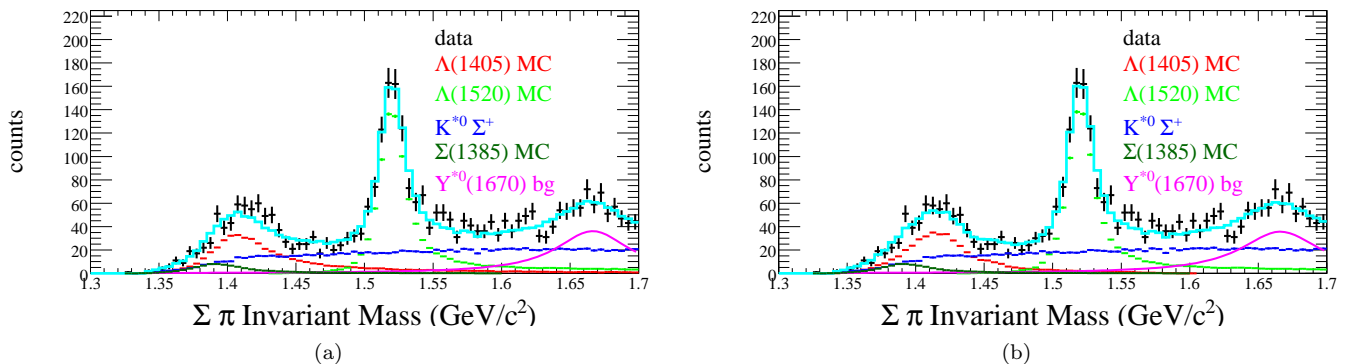
FIG. 2. (Color online) Fit result to the strong final state of $\Sigma^+\pi^-$ before MC iteration, for $W = 2.5$ GeV, $\cos\theta_{K^+}^{\text{c.m.}} = 0.35$. The data are the black crosses. (a) The initial fit. Each MC template is shown by a different color, as well as the Breit-Wigner function for the $Y^*(1670)$. The sum of the fit is shown in cyan. (b) Same as in (a), but after two iterations of the $\Lambda(1405)$ template to match the data.

$\Lambda(1405)$ and $\Lambda(1520)$ is that the particle yields for the former depended significantly on the final charge state ($\Sigma^+\pi^-$, $\Sigma^0\pi^0$, $\Sigma^-\pi^+$), while those for the latter did not, as will be seen later. When integrating over all production angles $\cos\theta_{K^+}^{\text{c.m.}}$, the mass distribution or "line shapes" in the charged decay modes of the $\Lambda(1405)$ differed, as detailed in Ref. [30]. In contrast, for this paper we take the summed yields across each $\Sigma\pi$ mass distribution and present the differential cross sections as a function of production angle.

Tests were carried out to verify that the $K^{*0}\Sigma^+$ background did not cause changes in the cross section or the line shapes of the hyperons. Indeed, no interference effects were seen in the photoproduction line shapes [30] or in the extracted differential cross sections, so that the incoherent sum used here was justified.

C. Acceptance and normalization

A large number of MC events were processed using the GEANT-based standard CLAS simulation package GSIM. The event generator used a bremsstrahlung photon energy distribution. The kaon production angle distributions were taken to have an empirical t-slope matching the one for ground state $K^+\Lambda$ photoproduction [33]. All (quasi-) two-body decays were taken to be isotropic in their own rest frames. The generated events were passed through the detector simulation, and particle momenta were smeared to match the actual data. In an earlier detailed analysis of the g11a data set [34], it was found that the trigger conditions for this run were not ideally simulated, so a momentum-dependent *ad hoc* trigger efficiency correction of $\sim 5\%$ was applied. After all corrections were made, the simulated events were passed through the same analysis procedures as the actual data.

TABLE I. The global systematic uncertainties in the experiment. They can be divided into yield extraction, acceptance, target characteristics, photon flux normalization, and branching ratios [26]. The total was calculated by adding the most typical values in quadrature.

Source	Value (%)
ΔTOF cuts	2–6
Confidence level on kinematic fit	3–12
Selection of intermediate hyperons	2–3
Target density	0.11
Target length	0.125
Photon normalization	7.3
Live-time correction	3
Photon transmission efficiency	0.5
$\Sigma^0(1385) \rightarrow \Sigma\pi, \Lambda\pi$	1.5
$\Lambda \rightarrow p\pi^-$	0.5
$\Sigma^+ \rightarrow p\pi^0, n\pi^+$	0.30
$\Sigma^- \rightarrow n\pi^-$	0.005
Total	11.6

A further small correction was applied for events with a Λ in the strong final state that compensated for decays that occurred outside the CLAS time-of-flight Start Counter, as described in Ref. [30].

The photon flux in each energy bin was determined so that the differential cross sections could be computed. This was done using the CLAS-standard method based on counting out-of-time electrons in the photon tagger within well-defined time windows. Also, a correction was made for the measured $\simeq 70\%$ transmission of photons from the tagger, through collimators, to the physics target. Other corrections were made to handle photon tagger counters not in the primary trigger, and for the overall measured $\sim 85\%$ DAQ live-time for this data set. Thus, the cross sections reported here are absolutely normalized. As mentioned previously, other published CLAS data sets used the same normalization procedures and have the same level of normalization uncertainty.

D. Systematic uncertainties

There were overall or global systematic uncertainties from the yield extraction and acceptance, flux normalization, and the line shape fitting procedures. These are discussed in Ref. [30] and at more length in Ref. [35]. For the final systematic uncertainty, the most typical global uncertainties were added in quadrature to yield a final value of 11.6%. A summary of each uncertainty is shown in Table I. The largest single contribution was from the overall flux normalization. This was monitored on an hour-by-hour basis by measuring the ω production yield [36], and the uncertainty for the normalization was determined to be 7.3%.

IV. RESULTS

A. Results for $\Sigma^0(1385)$

The $\Sigma^0(1385)$ differential cross section was determined through its dominant decay mode to $\Lambda\pi^0$, as discussed above, and corrected by the PDG branching fraction of 87% to arrive at the final results. The differential cross sections in 100-MeV-wide bins of W are shown in Fig. 3 as a function of center-of-mass kaon angles. They are forward peaked with a fairly smooth fall-off as a function of angle, but also with a moderate rise in the backward direction at higher energies. These are the hallmarks of t-channel dominated meson exchange in the production mechanism, with a hint of u-channel baryon exchange to account for the back-angle rise. The red curves shown are the calculation of Oh [37] based on the model of Ref. [10]. In general, the calculation matches the data extremely well at the higher energies, but undershoots the mid-angles at center-of-mass energies between 2.25 and 2.55 GeV. This may suggest that for $\Sigma^0(1385)$ photoproduction, besides the dominant t-channel exchange mechanism, there may be some resonant contribution.

The model of Ref. [10] is essentially a prediction based only on a preliminary total cross section measurement. In that model, several N^* resonances with one- and two-star ratings were included to produce the "peak" in the cross section near $E_\gamma = 2.0$ GeV. Our new differential cross section results should allow refinement of these estimates.

The only other data available are two data points from the LEPS Collaboration [24] at SPring-8, shown as green hollow circles at forward angles in the four lowest W bins. These two points are plotted twice each since they were obtained in wide energy bins of $1.5n < E_\gamma < 2.0$ GeV and $2.0 < E_\gamma < 2.4$ GeV. The LEPS data were taken at more forward angles than our measurements, and while the lower energy data is in fair agreement with our measurements, the higher energy point seems to be somewhat higher than expected from extrapolation of our results.

Figure 4 shows the differential cross section in just one bin of W. The acceptance of CLAS is such that there are holes in the forward and the backward directions. In order to estimate the total cross section an extrapolation into these regions was necessary. In the absence of a trusted theoretical model for this purpose, we averaged an array of plausible functions. The multiple lines in this figure show the *ad hoc* fits that were performed for this purpose. These were made in a purely empirical way in order to estimate how much variation can reasonably exist, subject to the constraint that the fits remained positive-definite and that the extrapolations were not unreasonably wild.

The functions, using $z = \cos\theta_{K^+}^{\mathrm{c.m.}}$ were:

1. absolute square of Legendre polynomials $P_l(z)$ with
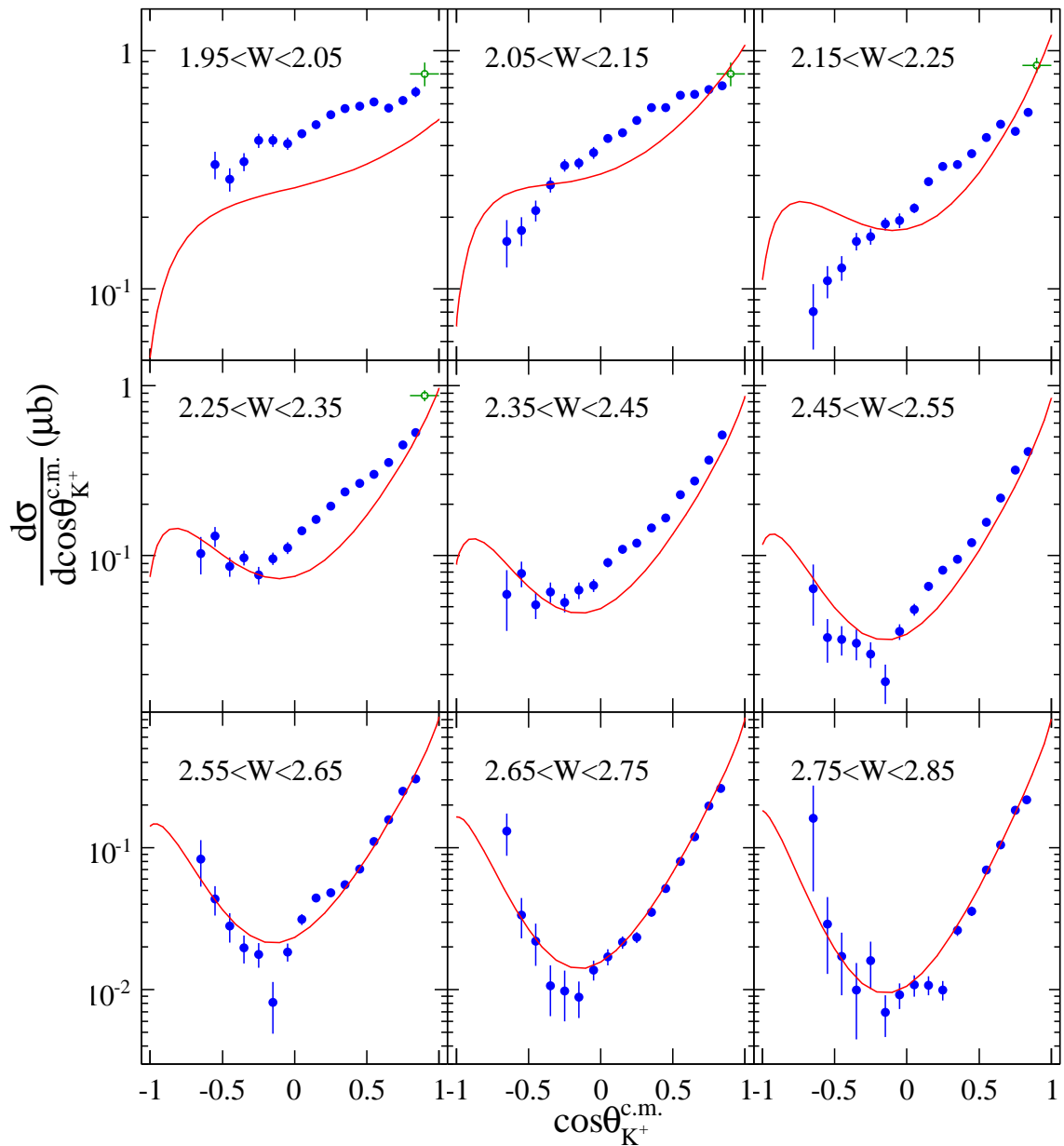
FIG. 3. (Color online) Differential cross section for $\gamma p \to K^+\Sigma^0(1385)$ for the indicated 100 MeV wide bins in W (GeV). The CLAS results are the filled blue points, with error bars that show the combined statistical and signal channel fit (see Fig. 1) uncertainties. The green hollow points are from LEPS [24]. The solid red lines are the model prediction of Ref. [10].

complex coefficients c_l given in the form of

$$f(z) = \left| \sum_{l=0}^{L} c_l P_l(z) \right|^2, \qquad (1)$$

with the maximum order L being either 2 or 3.

2. the $f(z)$ from Eq. (1) with an additive exponential of the form Ce^{-Dz} to account for the forward rise. In this case the maximum order used for the Legendre polynomials was $L = 1, 2, 3$.

3. the form of Eq. (1), with a multiplicative overall exponential function Ce^{-Dz}, with $L = 1, 2, 3$.

4. two exponentials $C_1 e^{-D_1 z}$ and $C_2 e^{+D_2 z}$ added to the form of Eq. (1), to take into account both the forward and the backward rises. The order used was $L = 2$.

Each of these fits was integrated to determine the span of variation that the total cross section could have. Figure 5 illustrates how this method of estimating the total cross section varied depending on the choice of fit function. We ascribe no physical interpretation to any of the fit func-

tions; they merely allowed us to estimate the total cross sections. We computed the weighted average of all the individual points at a given W and assigned that value as the total cross section, and used the standard deviation of those points as the estimate of the uncertainty on the total cross sections.
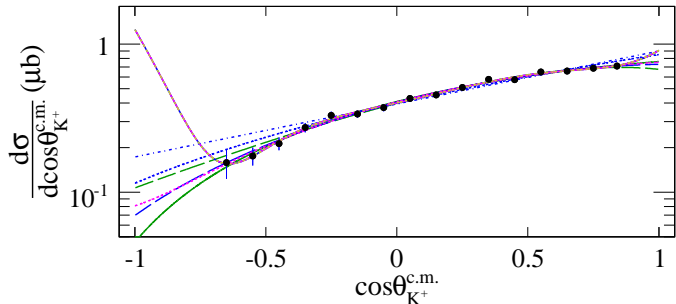

FIG. 4. (Color online) Differential cross section for $\gamma p \rightarrow K^+\Sigma^0(1385)$ with possible extrapolations in a single W bin for $2.05 \leq W \leq 2.15$ GeV. Some of the nine curves lie on top of each other. See text for discussion.
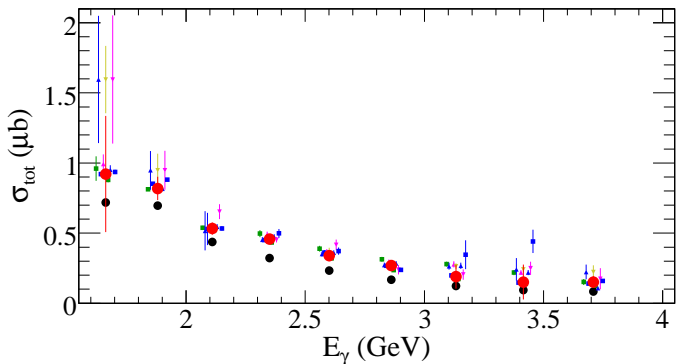

FIG. 5. (Color online) Total cross section of $\Sigma^0(1385)$ as a function of E_γ, showing at each E_γ the collection of alternative extrapolations of the differential cross sections tested. The lower black points show the summed unextrapolated data. The large red points show the averaged extrapolated values.

The final total cross section result for $\gamma p \rightarrow K^+\Sigma^0(1385)$ is shown in Fig. 6. The small blue points are the summed data across the production angles accessible in CLAS, while the large red points are the result of the extrapolations to all angles. For comparison, we see good agreement between these results and the much coarser, early bubble chamber data of Refs. [5–7]. The solid black curve is due to the calculation of Oh [37], and again there is very good agreement at the higher energies, but there is some disagreement in the region of $2.0 \leq E_\gamma \leq 2.5$ GeV.
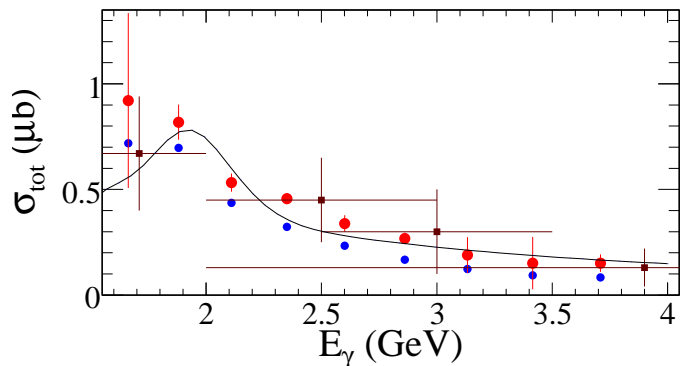
FIG. 6. (Color online) Total cross section for $\gamma p \rightarrow K^+\Sigma^0(1385)$ as a function of photon energy E_γ. The small blue points are the summed contribution from the measured range of angles in CLAS. The large red points are the extrapolated total cross sections using the method discussed in the text. The four dark brown square data points with cross-like error bars are bubble chamber data from Refs. [5–7]. The solid black curve shows the model of Ref. [10].

B. Results for $\Lambda(1520)$

As discussed in Sec. III B, the $\Lambda(1520)$ yields were obtained using template fits in each energy and angle bin. All charge combinations, $\Sigma^+\pi^-, \Sigma^-\pi^+$, and $\Sigma^0\pi^0$ were examined. For the Σ^+ decays, the two modes $p\pi^0$ and $n\pi^+$ could be compared for consistency. Figure 7 shows this comparison in a typical W bin. The two channels show good consistency. The lower gray band shows the angle-by-angle systematic discrepancy, computed as the difference between the measured final states with the summed statistical uncertainties subtracted in quadrature. This quantity is plotted when the difference between the data points is larger than the sum of the two error bars. Note that the vertical scale is logarithmic. The following results use the weighted average of the two Σ^+ final state measurements.

Each of the three $\Sigma\pi$ decay modes was reconstructed in the analysis, so next we compare these three modes for the $\Lambda(1520)$. This is shown in Fig. 8 for two typical bins in W. The agreement among the three decay modes is fair to good across the range of center-of-mass kaon production angles. In principle these should all be identical in the absence of interference among different isospin contributions to the reaction mechanism. This was true for the $\Lambda(1520)$, but as shown later, not for the $\Lambda(1405)$, where strong differences are seen depending on the $\Sigma\pi$ channel. It was assumed, for the $\Lambda(1520)$ therefore, that each decay mode contributes $1/3$ to the total decays to $\Sigma\pi$, and the measurements scaled accordingly and averaged in each bin over the measured channels. The overall branching fraction of 42% for $\Lambda(1520) \rightarrow \Sigma\pi$ was applied to obtain the final values of the differential cross section for the $\Lambda(1520)$.

The resultant differential cross section for the $\Lambda(1520)$
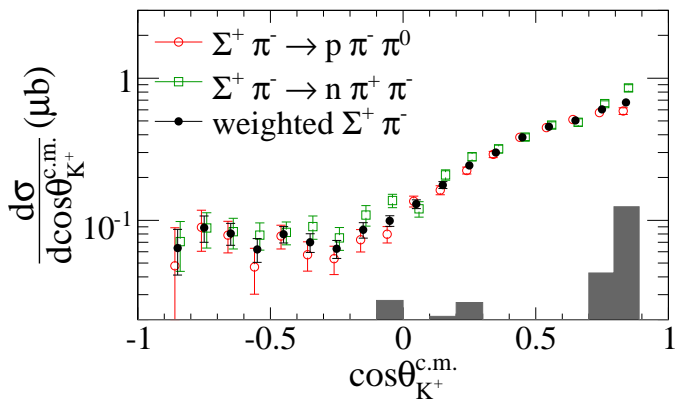
FIG. 7. (Color online) Comparison of the two $\Sigma^+\pi^-$ channels for the $\Lambda(1520)$ with $2.45 \leq W \leq 2.55$ GeV. The gray band is the estimated systematic discrepancy between measurements using the two reconstructed final states. Note the logarithmic vertical scale.
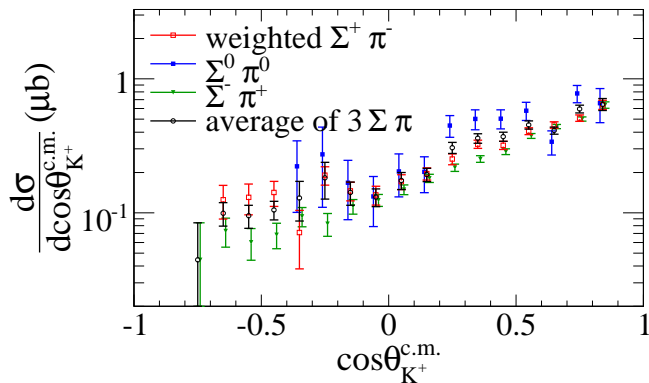
(a)
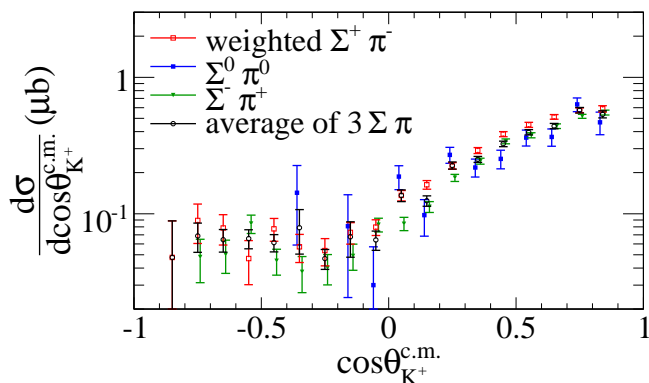
(b)

FIG. 8. (Color online) Comparison of the three $\Sigma\pi$ decay modes for the $\Lambda(1520)$ in two energy bins at (a) $2.05 \leq W \leq 2.15$ GeV and (b) $2.45 \leq W \leq 2.55$ GeV as a function of center-of-mass kaon angle. The data points have been shifted slightly to prevent overlaps, for clarity.

in a single typical W bin is shown in Fig. 9. As in Fig. 4, one sees that the CLAS acceptance did not extend to the extreme forward and backward kaon production angles, due to the openings in the spectrometer in those directions. We fitted a series of functions in the same manner as done previously for the $\Sigma^0(1385)$ discussed in Section IV A. We took the weighted average of all these variants and their standard deviation as the best estimated uncertainty for the total cross section.
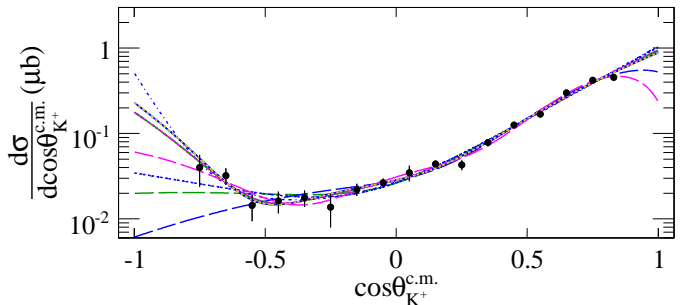
FIG. 9. (Color online) Differential cross section for $\gamma p \rightarrow K^+\Lambda(1520)$ with fit results to a single W bin for $2.75 \leq W \leq 2.85$ GeV. The various curves represent possible extrapolations to obtain the total cross section. Some of the nine curves lie on top of each other.

The final differential cross sections for the $\Lambda(1520)$ in all bins of W are shown in Fig. 10. Near threshold the CLAS cross section is fairly flat. Due to the $\Lambda(1520)$ threshold at 2.013 GeV, the lowest W bin was normalized using the uniform integrated photon flux between 2.020 GeV and 2.050 GeV, a 30 MeV wide region. The other bins are 100 MeV wide. There is an additional estimated $\pm36\%$ systematic scale uncertainty in this W bin due to the finite width of the hyperon, acceptance, and threshold effects. In the highest energy bin the cross section is quite forward peaked with a hint of plateauing toward the most forward angles. Also evident is that the cross section flattens or even rises slightly toward large angles. These are the qualitative hallmarks of t-channel dominance with at least two poles/trajectories at low $-t$ and possible $s-$ or u-channel baryon exchange at large angles.

For comparison with the CLAS results, the data from LEPS are shown. Ref. [13] measured the differential cross section in several final states using various methods that were presented as equivalently accurate. These points are shown as open squares in Fig. 10. In the threshold region, Ref. [14] measured the rapidly-rising differential cross section with finer energy binning than our present results. Points that overlap with our bins are shown as the open circles in Fig. 10. Agreement between CLAS and LEPS is good or very good across all overlapping bins.

The red solid curves are the model of Nam *et al.* [16] computed for the present kinematics [38]. No Regge contributions were included, and no K^* exchange in the t

channel. Also, the $\Lambda(1520)$ anomalous magnetic moment was set to zero, implying no u-channel exchanges. This leaves the dominant contact term interaction as well as small contributions from t and s channel Born terms. Note that this model was developed to match the scant higher energy data from Ref. [12]. This is seen in Fig. 11, where the red solid curve comes closest to the Ref. [12] data set but is significantly higher than the new CLAS results. This model overestimates the cross section and lacks sufficient strength at large angles.

The black dashed curves in Fig. 10 show the model prediction of He and Chen [19] computed for the present kinematics [39]. Evidently this model is a closer match to the new data, but the comparison is not perfect. It captures the slight rise at backward angles and is mostly closer in magnitude to the data. It also tends to follow the flattening of the total cross section at forward angles. This model includes K^* exchange, and although this is more important at higher energies, it may help reproduce the forward-angle behavior we see. This model also includes the s-channel $N(2080)D_{13}$ resonance that was quite significant when matching the data of Kohri et $al.$ from LEPS [14]. (See also the earlier work in Ref. [40].) This resonance is also responsible for the fairly narrow peak in the total cross section near 2 GeV shown in Fig. 11. We can conclude that this model, using several additional interaction elements compared to Nam et $al.$ [16], is able to come closer to reproducing the present differential and total cross section data for the $\Lambda(1520)$.

Figure 11 shows the total photoproduction cross section for the $\Lambda(1520)$. The recent SAPHIR data [20] is in rather strong disagreement with the data from SLAC/LAMP2 [12]. The new CLAS results lie almost exactly between these two measurements. The small blue data points show the CLAS data summed over the useful acceptance of the detector, and the larger solid red points show the extrapolated total cross section. The model curves correspond to those of Fig. 10.

C. Results for $\Lambda(1405)$

The case of the $\Lambda(1405)$ is somewhat different from the others because each of the $\Sigma\pi$ charged final states yields a different cross section. In our previous paper [30] this was traced to the fact that there is considerable interference of an $I = 1$ $J^P = 1/2^-$ amplitude with the $I = 0$ $J^P = 1/2^-$ amplitude that, by definition, represents the $\Lambda(1405)$. In Refs. [30] and [41], isospin decompositions were done in an attempt to separate those amplitudes as a function of the $\Sigma\pi$ mass and of W. In those articles the data were integrated over all kaon production angles, but in the present situation we wish to extract the cross section as a function of kaon production angle while integrating over the $\Sigma\pi$ mass distributions. Unfortunately, with the statistics available in this measurement it was not possible to do the isospin decomposition in each energy and angle bin separately. Instead, we present the

results when integrating the $\Sigma\pi$ mass range from threshold up to 1.5 GeV. Thus, we say that this experiment has measured the cross section in the "region" of the $\Lambda(1405)$, without explicit separation of the isospin amplitudes.

As in Sec. IV B for the case of the $\Lambda(1520)$, there were two decay modes for reconstructing the Σ^+. A sample comparison of these two modes is shown in Fig. 12. The agreement between the decay modes was usually good to very good. In each case, the yield of what we nominally call the $\Lambda(1405)$ was taken from the line shape templates in the relevant mass range discussed in Sec. III B. The gray systematic error band is the difference between the measured values with the summed point-to-point uncertainties subtracted off in quadrature. These two measurements were then averaged together to give the cross section in the $\Sigma^+\pi^-$ decay mode.

Comparison of the $\Sigma^\pm\pi^\mp$ and $\Sigma^0\pi^0$ decay modes of the $\Lambda(1405)$ mass region is shown in Figs. 13 and 14 for all bins in W. In the lower W bins there are very significant differences between the measured cross sections. Below about $W = 2.3$ GeV there is clearly some additional dynamics present causing the charge states to have quite different cross sections. We interpret this as being due to the interference of $I = 0$ and $I = 1$ amplitudes in the production mechanism in the $\Lambda(1405)$ mass range. The steep drop in the $\Sigma^0\pi^0$ cross section at large angles for the lower W bins was checked and found to be correct in this analysis. Toward the higher end of the W range the three cross sections tend to merge together into a characteristic forward peak, indicating t-channel dominance in the reaction mechanism.

At present there is no model calculation available that can explain this interference effect. Due to the lower c.m. momenta at lower W, one may speculate that the electromagnetic and hadronic interactions have more time to develop at lower W, hence showing more interference effects. Below $W = 2.3$ GeV the mean $\Lambda(1405)$ decay distance is less than the incoming photon wavelength.

To combine these three channels into one effective cross section for the $\Lambda(1405)$ mass region, we simply added the three components together. In Ref. [30] it was shown that if t_0 is the amplitude for the $I = 0$ production and if t_1 is the amplitude for the $I = 1$ mechanism that interferes with it, then the sum of the three decay modes is proportional to $|t_0|^2 + |t_1|^2$, with cancellation of the interference cross terms.

The resulting summed differential cross sections for the $\Lambda(1405)$ mass range are shown in Fig. 15. The overall trends are quite similar to the other two hyperons. We will make a direct comparison later. The $\Sigma^0\pi^0$ cross section was not measured in the forward-most angle bin for $W = 2.00$ GeV, as seen in Fig. 13. The summation used the neighboring value for this datum, with an error bar enlarged to the size of the difference between the two neigboring points.

The only data comparison available is the LEPS Collaboration result by Niiyama et $al.$ [24] in the lowest W bins. Their two data points are plotted twice each since
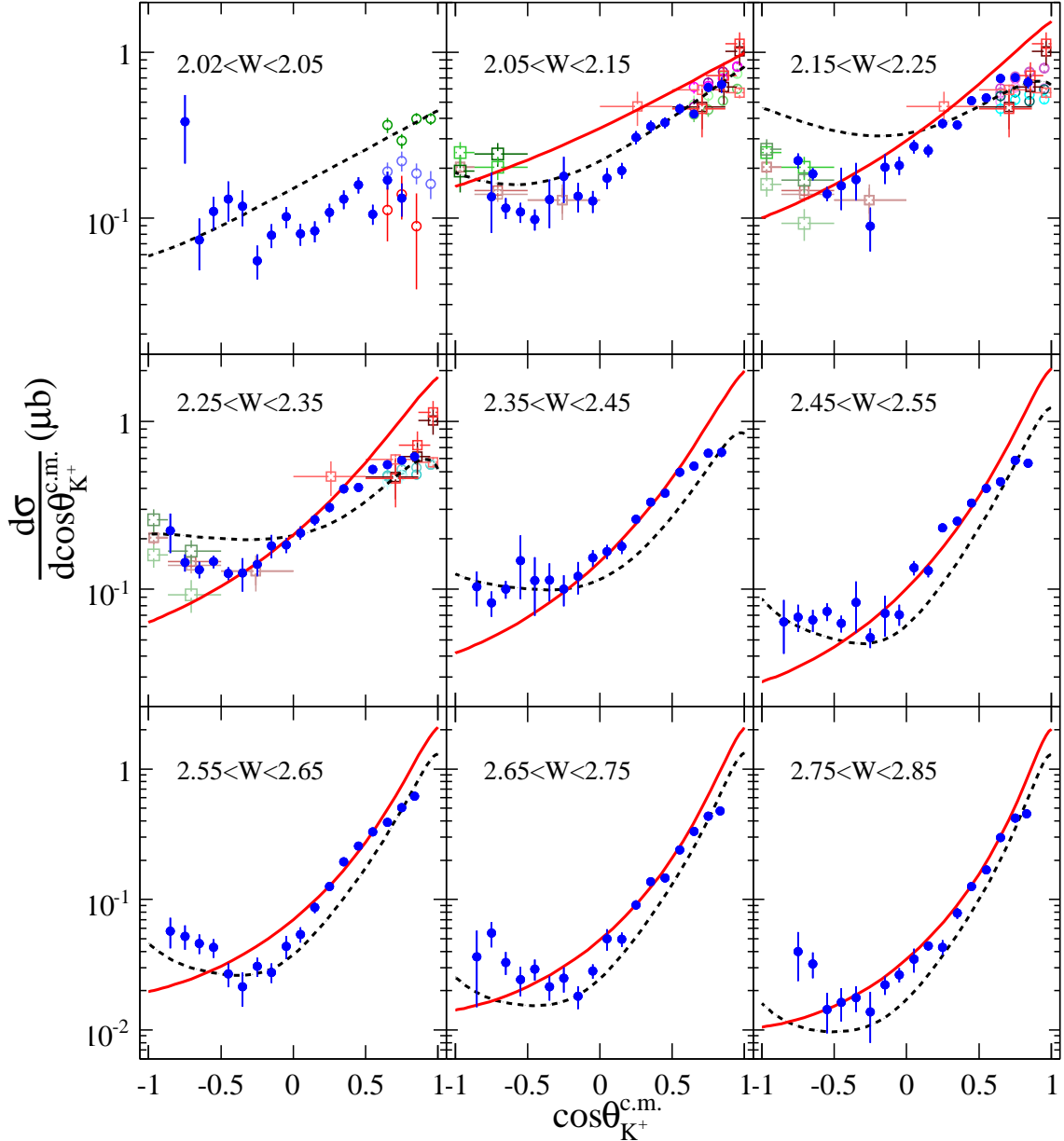
FIG. 10. (Color online) Differential cross section for $\gamma p \to K^+\Lambda(1520)$ for nine bins in center-of-mass energy W (GeV). The solid blue circular points are the measured CLAS data. Measurements from LEPS are shown by the various colored hollow square points [13]. The hollow circular points show separate LEPS results [14]; in the lowest W bin they are for $W = 2.01$ GeV (red), 2.03 GeV (blue), and 2.05 GeV (green). The lowest W bin is 30 MeV wide, while the others are all 100 MeV wide. The black dashed curve is the model calculation by He *et al.* [19], while the red solid curve is the model calculation by Nam *et al.* [16]. Note that the first bin in W is 30 MeV wide while the others are 100 MeV wide.

their energy bins were quite wide compared to ours. The claim made in that paper was that the ratio of $\Lambda(1405)$ to $\Sigma^0(1385)$ drops from 0.54 ± 0.17 to 0.084 ± 0.076 between their two energy bins. The CLAS results do not support the LEPS observation. For W between 2.15 and 2.35 GeV the CLAS cross sections are about a factor of six larger than those of the previous experiment.

A recent prediction for the $\Lambda(1405)$ photoproduction cross section due to Nam *et al.* [27] is plotted in Fig. 15.

In their effective Lagrangian model the s-channel Born term is dominant. There is interference with K^* exchange, and the three curves stem from letting $g_{K^*N\Lambda^*}$ take the values 0 (solid red), $+3.18$ (dotted red), or -3.18 (dashed red). Evidently, this model omits a very significant t-channel-like piece of the reaction mechanism. Also in Fig. 15, in the bin centered at $W = 2.0$ GeV, we show in dashed magenta the flat curve from Williams, Ji, and Cotanch [28]; this was their prediction based on crossing-
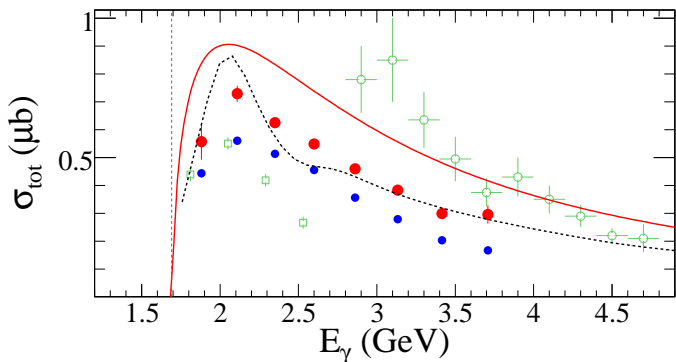
FIG. 11. (Color online) Total cross section of $\Lambda(1520)$ as a function of E_γ. The small blue points are the CLAS data summed over the acceptance of the detector, while the larger solid red points show the extrapolation over all space. The error bars are the combined statistical and extrapolation uncertainties. The dashed black curve is a calculation by He *et al.* [19] and the solid red curve is a calculation by Nam *et al.* [16]. The green hollow squares are measurements by SAPHIR [20], and the green hollow circles are measurements from SLAC/LAMP2 [12].
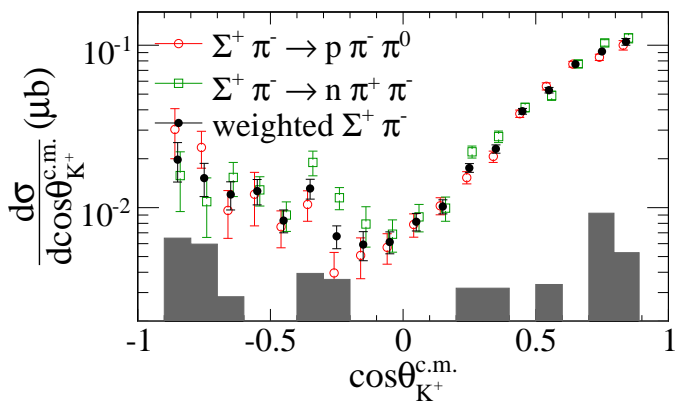
FIG. 12. (Color online) Comparison of the two Σ^+ decay modes for the $\Lambda(1405)$ with $2.45 \leq W \leq 2.55$ GeV. The gray band is the estimated systematic discrepancy between measurements using the two reconstructed final states. The points have been shifted for visual clarity.

symmetry and duality constraints using no intermediate N^* resonances, and using their lowest estimate for the $KN\Lambda(1405)$ coupling constant. Evidently this prediction of the cross section was too large by at least a factor of two.

Ref [30] presents the $\Sigma\pi$ mass distributions ("line shapes") of the $\Lambda(1405)$ region. It was not possible to do a kinematic fit in the $\Sigma^0\pi^0$ analysis to achieve background rejection as good as for the $\Sigma^\pm\pi^\mp$ channels. Some $\cos\theta_{K^+}^{c.m.}$ angle-integrated line shape fits had considerable possibly-incoherent background due to particle misidentification, higher mass hyperons, or other sources. (See Figs. 20, 21, and 22 in Ref [30].) For the present differential cross section analysis, this background could not be

measured separately in each angle bin because of statistical limitations. In Ref [30] the model assumed a linear background from threshold up to 1.6 GeV, but in fact we do not have definite knowledge of the background that may have escaped our simulations near 1.6 GeV, nor its shape under the $\Lambda(1405)$. How this background is distributed in angle also cannot be determined accurately from our measurements. Only an experiment with even better $\Sigma^0\pi^0$ identification will be able to clarify this point. In this article we do not subtract any estimated background from the $\Lambda(1405)$ cross sections.

Figure 16 shows the total cross section. The small black data points show the CLAS data summed over the useful acceptance of the detector, and the larger solid red points again show the extrapolated total cross section. The curves correspond to calculations of Nam *et al.* [38]. Clearly, the calculations do not match the overall scale of the cross sections, nor the dominant forward peaking behavior.

D. Comparison of results

Figure 17 shows the differential cross sections for the $\Sigma^0(1385)$, $\Lambda(1520)$, and the $\Lambda(1405)$ region on a single plot. It is evident that the overall behavior of the three hyperons is quite similar. Near threshold the respective phase space volumes differ and the magnitudes differ greatly. But away from threshold, each of them falls with increasing kaon production angle and then rises again in the backward hemisphere. The $\Lambda(1405)$ region, despite its peculiar charge-dependent line shapes, has a qualitatively similar differential cross section behavior as the $\Sigma^0(1385)$ and $\Lambda(1520)$.

The total cross sections for all three hyperons are shown together in Fig. 18. The fall-offs after the initial rise of the cross sections are similar for the $\Sigma^0(1385)$ and the $\Lambda(1520)$, and slightly slower for the $\Lambda(1405)$. The $\Lambda(1405)$ is photoproduced with about half the strength of its isospin partner $\Lambda(1520)$, while the $\Sigma^0(1385)$ lies in between. Recall, however, that the branching fraction of the $\Lambda(1520)$ to $\Sigma\pi$ is 42%, since it lies above the $N\bar{K}$ threshold, while the below-threshold $\Lambda(1405)$ decays 100% to $\Sigma\pi$. One can therefore say that the $\Lambda(1405)$ and the $\Lambda(1520)$ have close to equal strength for decaying to these final states. We plot for comparison the total photoproduction cross sections of the ground state Λ and Σ^0 [33]. Above about 2.1 GeV, we see that cross sections for the excited hyperons differ from those of the ground state hyperons by factors of less than two to three.

V. CONCLUSIONS

We have measured for the first time in a single experiment the differential cross sections for photoproduction of the $\Sigma^0(1385)$, $\Lambda(1520)$, and $\Lambda(1405)$. The $\Sigma^0(1385)$ was measured through its dominant decay mode to $\Lambda\pi^0$,
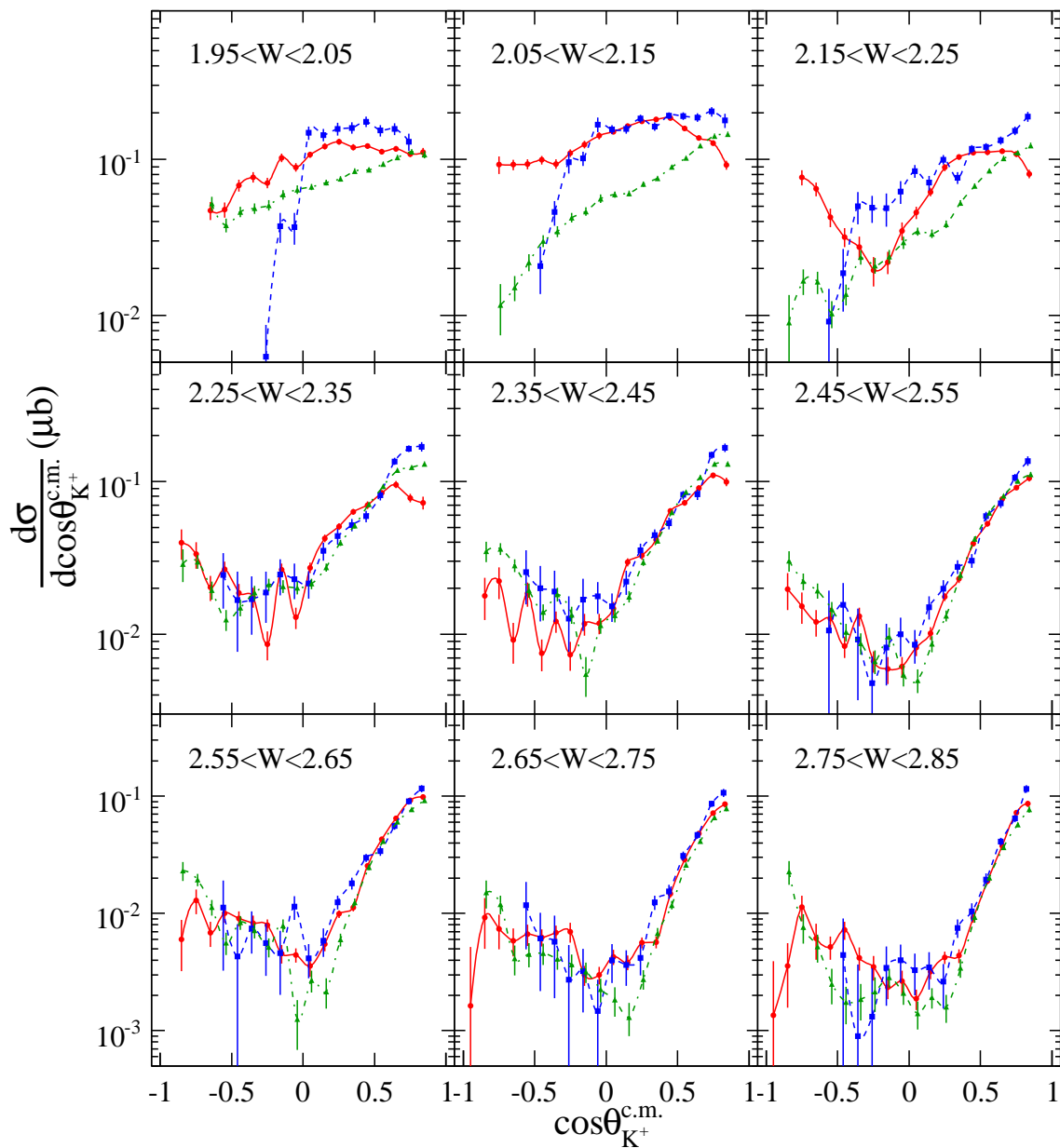
FIG. 13. (Color online) Differential cross sections for $\gamma p \rightarrow K^+ Y^*$ in the $\Lambda(1405)$ mass region from threshold to 1.5 GeV/c^2 for each of the three $\Sigma\pi$ charge states. The ranges of center-of-mass energies W (GeV) are indicated. The $\Sigma^+\pi^-$ channel is shown as red circles/solid line, the $\Sigma^0\pi^0$ channel is shown as blue squares/dashed line, and the $\Sigma^-\pi^+$ channel is shown as green triangles/dot-dashed line. The curves are simply spline fits to guide the eye.

while the other two were measured through all three $\Sigma\pi$ decay combinations. They are all of similar size and angular dependence, and summarized in Figs. 17 and 18. However, the $\Lambda(1405)$ region is qualitatively different because the angular dependencies of the three charge combinations are quite different, as shown in Fig. 13. This is naturally explained if one allows strong isospin interference in the production of the $\Sigma\pi$ final state in the $\Lambda(1405)$ mass region.

This is of particular interest to chiral unitary models that describe the $\Lambda(1405)$ in terms of a two-pole $I = 0$ structure (for a recent review, see Ref. [42]). The strong angular and energy dependence of the production is a challenge to models that so far use only a Weinberg-Tomozawa-type contact interaction to generate the $\Lambda(1405)$. If it is the case that significant $I = 1$ strength is present in the $\Lambda(1405)$ production mechanism, it will be more difficult to develop a complete theory of its creation, at least in photoproduction.

Existing model calculations compared to the present results are moderately successful at reproducing the differential cross sections of the $\Sigma^0(1385)$ and $\Lambda(1520)$. The
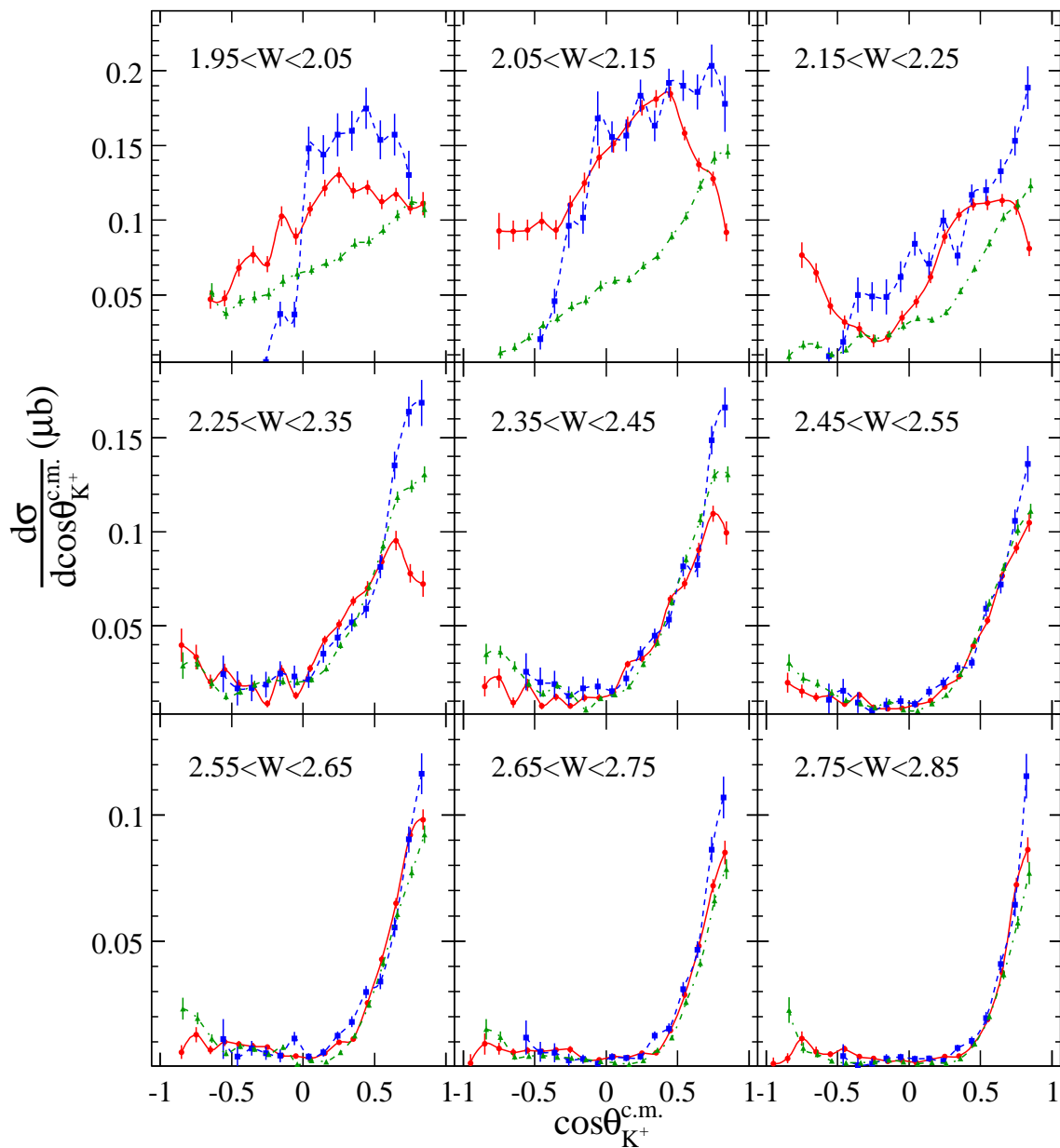
FIG. 14. (Color online) Differential cross sections for $\gamma p \rightarrow K^+ Y^*$ in the $\Lambda(1405)$ mass region for each of the three $\Sigma\pi$ charge states. The ranges of center-of-mass energies W (GeV) are indicated. Same as previous figure, but on a linear vertical scale to emphasize the differences in lower W.

models were all effective Lagrangian calculations with semi-empirical fits of coupling constants to match the very sparse previous data. These new data will, however, allow these and other models to be refined in the future. In particular, the role of K^* and N^* contributions to the reaction mechanisms may now be more closely studied. Much more work is needed to model the $\Lambda(1405)$.

In the future it would be helpful to get much higher statistics for photoproduction of the $\Lambda(1405)$ to make it possible to do an isospin analysis in each energy and angle bin separately. This is necessary to unravel the nature of this state in more detail. Nevertheless, the present study has provided the first comprehensive look at the group of low-lying excited hyperons in photoproduction. Theoretical understanding of their production and internal structure should be improved as a result.
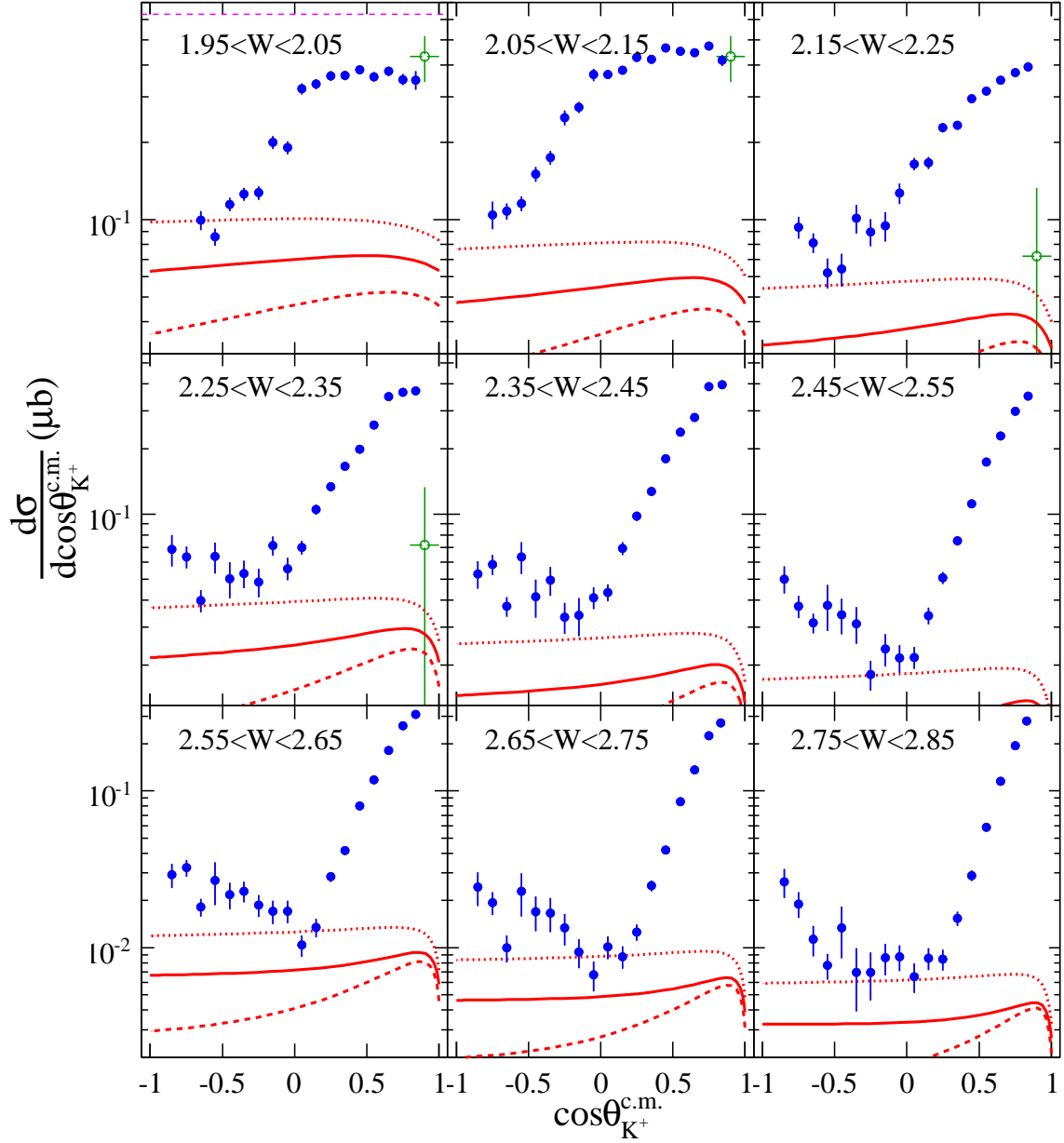
FIG. 15. (Color online) Differential cross sections for $\gamma p \rightarrow K^+ Y^*$ for the $\Lambda(1405)$ mass region in the indicated 100 MeV wide bins in W (GeV). The CLAS data (solid blue points) have been summed over the three $\Sigma\pi$ decay modes. The error bars combine statistical and systematic fitting uncertainties. The forward-most datum in the lowest W bin used an estimated value for the $\Sigma^0\pi^0$ cross section. The green hollow circle points are from Ref. [24]. The red curves are from Ref. [38], based on the model of Ref. [27] discussed in the text, while the flat dashed magenta line in the $W = 2.0$ GeV panel is the prediction from Ref. [28].

[1] N. Isgur and G. Karl, Phys. Rev. **D18**, 4187 (1978).

[2] S. Capstick and W. Roberts, Prog. Part. Nucl. Phys. **45**,
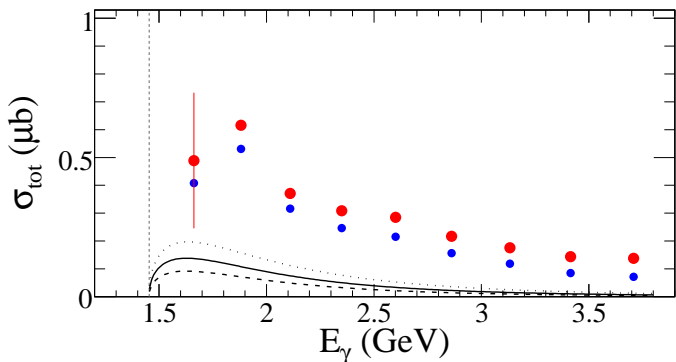
FIG. 16. (Color online) Total cross section of $\Lambda(1405)$ mass region versus E_γ. The small blue points show the summed measured data from the CLAS detector, while the large red points show the extrapolation to all angles. The error bars are combined statistical and fitting uncertainties. The vertical dashed line shows the reaction threshold. The black curves are a calculation by Nam *et al.* based on [27], with the variable $g_{K^*N\Lambda^*}$ set to 0 (solid), +3.18 (dotted), or −3.18 (dashed).

S241 (2000).

[3] R. H. Dalitz and S. F. Tuan, Phys. Rev. Lett. **2**, 425 (1959).

[4] R. H. Dalitz and S. F. Tuan, Annals Phys. **10**, 307 (1960).

[5] R. Erbe *et al.* (Aachen-Berlin-Bonn-Hamburg-Heidelberg-Muenchen Collaboration,), Phys. Rev. **188**, 2060 (1969).

[6] R. Erbe *et al.* (Aachen-Berlin-Bonn-Hamburg-Heidelberg-Muenchen Collaboration,), Nuovo Cimento **49**, 504 (1967).

[7] H. Crouch *et al.* (Cambridge Bubble Chamber Group), Phys. Rev. **156**, 1426 (1967).

[8] L. Guo and D. P. Weygand (CLAS Collaboration), (2006), *Proceedings of the Internatinal Workshop on the Physics of Excited Baryons (NSTAR2005)*, edited by S. Capstick, V. Crede, and P. Eugenio (World Scientific, Singapore, 2006), arXiv:0601010.

[9] K. Hicks *et al.* (LEPS Collaboration), Phys. Rev. Lett. **102**, 012501 (2009).

[10] Y. Oh, C. M. Ko, and K. Nakayama, Phys. Rev. **C77**, 045204 (2008).

[11] A. Boyarski, R. E. Diebold, S. D. Ecklund, G. Fischer, Y. Murata, *et al.*, Phys. Lett. **B34**, 547 (1971).

[12] D. Barber, J. Dainton, L. Lee, R. Marshall, J. Thompson, *et al.*, Z. Phys. **C7**, 17 (1980).

[13] N. Muramatsu, J. Chen, W. Chang, D. Ahn, J. Ahn, *et al.* (LEPS Collaboration), Phys. Rev. Lett. **103**, 012001 (2009).

[14] H. Kohri *et al.* (LEPS Collaboration), Phys. Rev. Lett. **104**, 172001 (2010).

[15] S.-I. Nam, A. Hosaka, and H.-C. Kim, Phys. Rev. **D71**, 114012 (2005).

[16] S.-I. Nam and C.-W. Kao, Phys. Rev. **C81**, 055206 (2010).

[17] A. Titov, B. Kampfer, S. Daté, and Y. Ohashi, Phys. Rev. **C74**, 055206 (2006).

[18] A. Sibirtsev, J. Haidenbauer, S. Krewald, U.-G. Meissner, and A. Thomas, Eur. Phys. J. **A31**, 221 (2007).

[19] J. He and X.-R. Chen, Phys. Rev. **C86**, 035204 (2012).

[20] F. Wieland *et al.* (SAPHIR Collaboration), Eur. Phys. J. **A47**, 47 (2011), Erratum: **A47**, 133 (2011).

[21] N. Mistry, S. Mori, D. Sober, and A. Sadoff, Phys. Lett. **24B**, 528 (1967).

[22] W. Blanpied, J. Greenberg, V. Hughes, P. Kitching, and D. Lu, Phys. Rev. Lett. **14**, 741 (1965).

[23] S. Barrow *et al.* (CLAS Collaboration), Phys. Rev. **C64**, 044601 (2001).

[24] M. Niiyama *et al.* (LEPS Collaboration), Phys. Rev. **C78**, 035202 (2008).

[25] R. Schumacher and M. Sargsian, Phys. Rev. **C83**, 025207 (2011).

[26] J. Beringer *et al.* (Particle Data Group), Phys. Rev. **D86**, 010001 (2012).

[27] S.-I. Nam, J.-H. Park, A. Hosaka, and H.-C. Kim, J. Korean Phys. Soc. **59**, 2676 (2011).

[28] R. Williams, C. Ji, and S. Cotanch, Phys. Rev. **C43**, 452 (1991).

[29] J. C. Nacher, E. Oset, H. Toki, and A. Ramos, Phys. Lett. **B455**, 55 (1999).

[30] K. Moriya, R. A. Schumacher, *et al.* (CLAS Collaboration), Phys. Rev. **C87**, 035206 (2013).

[31] D. I. Sober *et al.*, Nucl. Instrum. Meth. **A440**, 263 (2000).

[32] B. A. Mecking *et al.* (CLAS Collaboration), Nucl. Instrum. Meth. **A503**, 513 (2003).

[33] R. Bradford *et al.* (CLAS Collaboration), Phys. Rev. **C73**, 035202 (2006).

[34] M. Williams, Thesis, Carnegie Mellon University (2007), available online at http://www.jlab.org/Hall-B/general/clas_thesis.html.

[35] K. Moriya, Thesis, Carnegie Mellon University (2010), available online at http://www.jlab.org/Hall-B/general/clas_thesis.html.

[36] M. Williams *et al.* (CLAS Collaboration), Phys. Rev. **C80**, 065208 (2009).

[37] Y. Oh, Private communication.

[38] S.-I. Nam, Private communication.

[39] J. He, Private communication.

[40] J. Xie and J. Nieves, Phys. Rev. **C82**, 045205 (2010).

[41] R. A. Schumacher and K. Moriya, (2013), "Nucl. Phys. A (in press), Proceedings of the XI International Conference on Hypernuclear and Strange Particle Physics, Barcelona, Spain, Oct. 2012", arXiv:nucl-ex/1303.0860, http://dx.doi.org/10.1016/j.nuclphysa.2013.03.003.

[42] T. Hyodo and D. Jido, Prog. Part. Nucl. Phys. **67**, 55 (2012).

[43] The CLAS Database collects all data from CLAS. It is reachable via http://clasweb.jlab.org/physicsdb.

[44] Durham Database Group, Durham University(UK); http://durpdg.dur.ac.uk/HEPDATA/.

[45] Text file available by sending an email request to schumacher@cmu.edu.

Appendix: Numerical Results

The total cross section results from the present work are given in Table II. Each row corresponds to a given photon energy and gives the corresponding result for $\Sigma(1385)$, $\Lambda(1405)$, and $\Lambda(1520)$. The differential cross section results from the present work are given Table III. Each row corresponds to a given energy bin W and c.m.
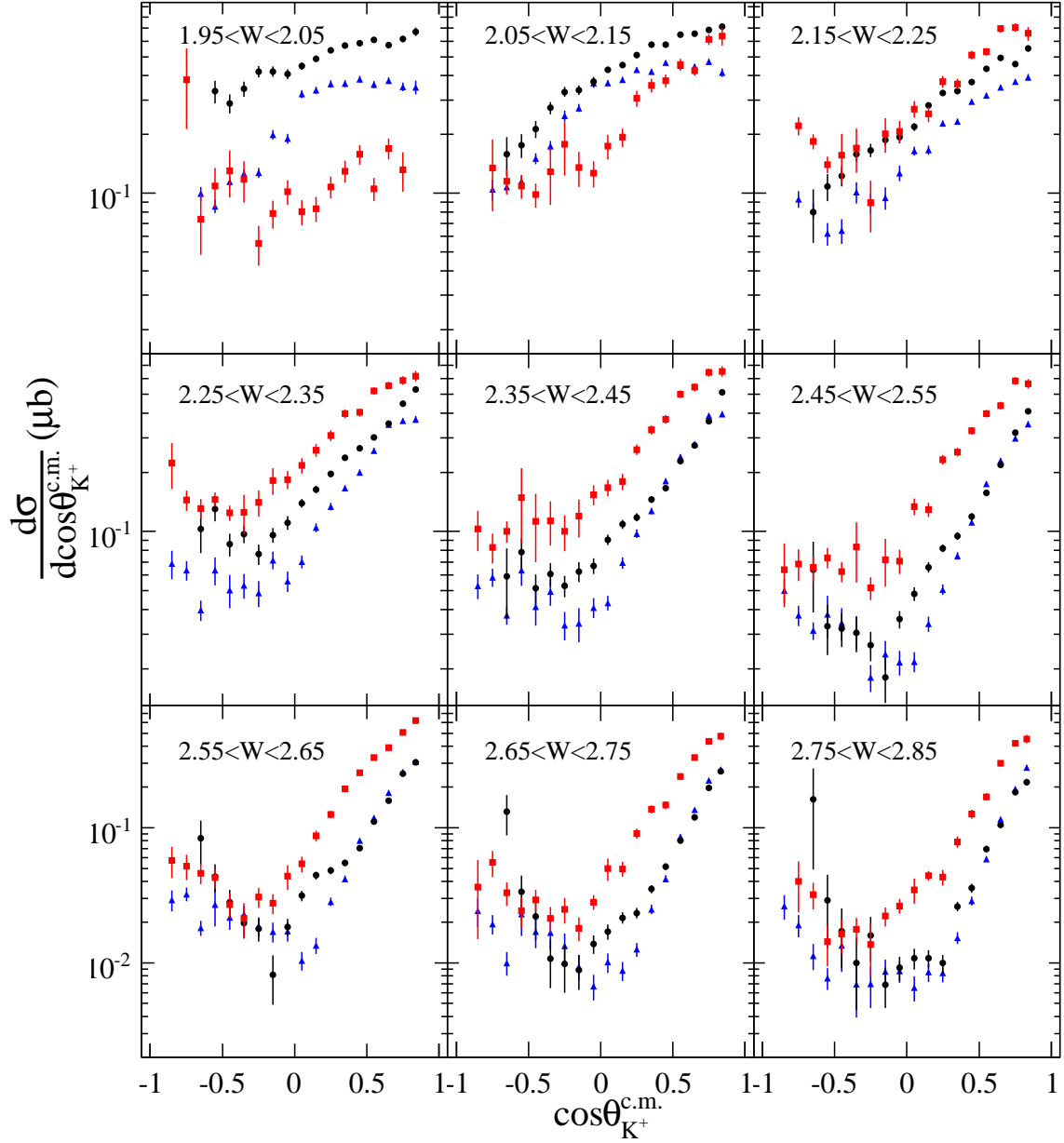
FIG. 17. (Color online) Comparison of the differential cross sections of the $\Sigma^0(1385)$ (black circles), $\Lambda(1405)$ (blue triangles), and $\Lambda(1520)$ (red squares) as a function of kaon production angle $\cos\theta_{K^+}^{\text{c.m.}}$ for each 100 MeV wide bin in energy W (GeV). (For the $\Lambda(1520)$ the threshold bin has $2.02 \leq W \leq 2.05$ GeV.)

kaon production angle $\cos\theta_{K^+}^{\text{c.m.}}$ for cross sections in the form $d\sigma/d\cos\theta_{K^+}^{\text{c.m.}}$. The quoted uncertainties are the statistical errors resulting from the yield fitting, acceptance calculation, photon normalization, and the extrapolation to full acceptance. Systematic uncertainties were discussed in the main text. A zero value for a cross section means no data point was extracted at that energy. Electronic tabulations of the results are available from several archival sources: Refs. [43], [44], [45].
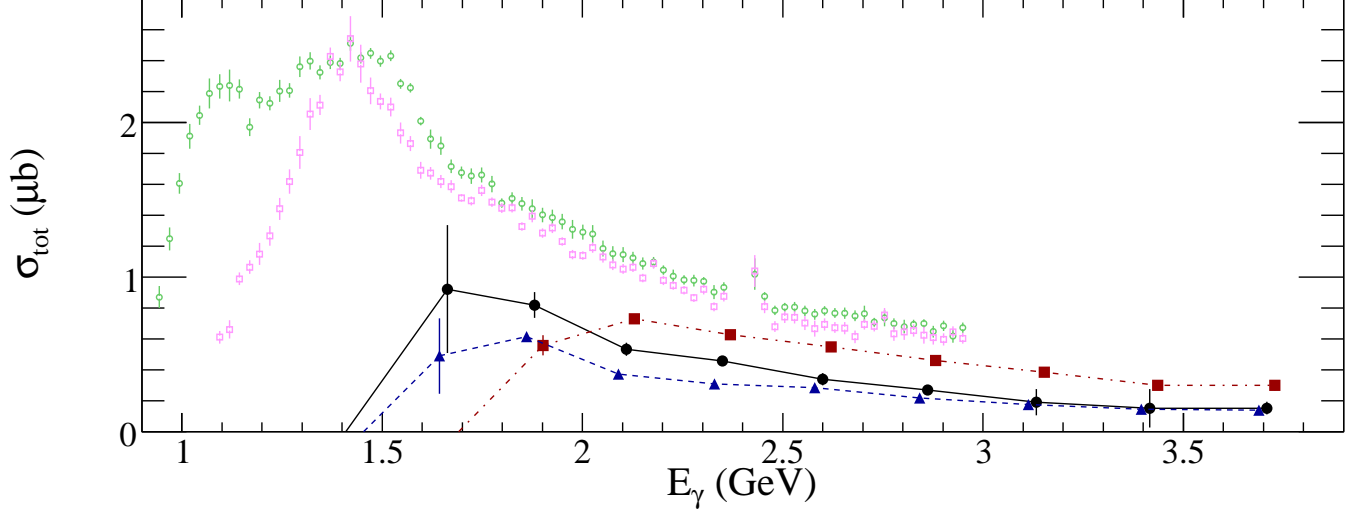
FIG. 18. (Color online) Comparison of total cross sections for the $\Sigma^0(1385)$ (black circles, solid line), $\Lambda(1405)$ (blue triangles, dashed line), and $\Lambda(1520)$ (red squares, dot-dashed line) vs. E_γ. The points for the $\Lambda(1405)$ and $\Lambda(1520)$ have been offset by 20 MeV for visual clarity. The open green circles and open magenta squares are the ground state Λ and Σ^0 total cross sections, respectively, from Ref. [33].

TABLE II. Results of CLAS measurements of $\gamma + p \rightarrow K^+ + Y^*$. The columns marked $\sigma_{\rm tot}$ are the total cross sections for the $\Sigma^0(1385)$, $\Lambda(1405)$, and $\Lambda(1520)$, respectively, while the columns marked "$\pm$" are the associated standard statistical uncertainties. The cross section units are in μb.

Index	E_γ (GeV)	$\Sigma^0(1385)$		$\Lambda(1405)$		$\Lambda(1520)$	
		σ_{tot}	$\pm$	σ_{tot}	$\pm$	σ_{tot}	$\pm$
1)	1.662	0.921	0.414	0.489	0.244	0.000	0.000
2)	1.881	0.818	0.083	0.615	0.008	0.557	0.065
3)	2.110	0.532	0.043	0.371	0.005	0.729	0.029
4)	2.350	0.457	0.026	0.309	0.011	0.625	0.015
5)	2.600	0.339	0.039	0.285	0.008	0.549	0.014
6)	2.862	0.268	0.027	0.216	0.008	0.460	0.015
7)	3.133	0.189	0.085	0.176	0.014	0.383	0.017
8)	3.416	0.151	0.124	0.144	0.014	0.299	0.016
9)	3.709	0.151	0.041	0.138	0.010	0.297	0.032

TABLE III: Results of CLAS measurements of $\gamma + p \rightarrow K^+ + Y^*$. Most energy bins are 100 MeV wide in W, centered on the value given in the second column. The threshold W bin for the $\Lambda(1520)$ is only 30 MeV wide. Most angle bins are 0.1 wide in $\cos\theta_{K^+}^{\mathrm{c.m.}}$, centered on the value given in the third column. The columns marked $d\sigma/d\cos\theta_{K^+}^{\mathrm{c.m.}}$ are the differential cross sections for the $\Sigma^0(1385)$, $\Lambda(1520)$, and $\Lambda(1405)$, respectively, while the columns marked "$\pm$" are the associated total point-to-point uncertainties. The cross section units are in μb.

Index	W (GeV)	$\cos\theta_{K^+}^{\mathrm{c.m.}}$	$\Sigma^0(1385)$ $d\sigma/d\cos\theta_{K^+}^{\mathrm{c.m.}}$	$\pm$	$\Lambda(1520)$ $d\sigma/d\cos\theta_{K^+}^{\mathrm{c.m.}}$	$\pm$	$\Lambda(1405)\rightarrow\Sigma^+\pi^-$ $d\sigma/d\cos\theta_{K^+}^{\mathrm{c.m.}}$	$\pm$	$\Lambda(1405)\rightarrow\Sigma^0\pi^0$ $d\sigma/d\cos\theta_{K^+}^{\mathrm{c.m.}}$	$\pm$	$\Lambda(1405)\rightarrow\Sigma^-\pi^+$ $d\sigma/d\cos\theta_{K^+}^{\mathrm{c.m.}}$	$\pm$
1)	2.000	-0.85	0.0000	0.0000			0.0000	0.0000	0.0000	0.0000	0.0000	0.0000
2)	2.000	-0.75	0.0000	0.0000			0.0000	0.0000	0.0000	0.0000	0.0000	0.0000
3)	2.000	-0.65	0.0000	0.0000			0.0471	0.0062	0.0000	0.0000	0.0523	0.0056
4)	2.000	-0.55	0.3327	0.0440			0.0478	0.0053	0.0000	0.0000	0.0379	0.0039
5)	2.000	-0.45	0.2887	0.0324			0.0683	0.0058	0.0000	0.0000	0.0462	0.0037
6)	2.000	-0.35	0.3424	0.0299			0.0771	0.0059	0.0000	0.0000	0.0486	0.0039
7)	2.000	-0.25	0.4201	0.0290			0.0707	0.0054	0.0054	0.0033	0.0509	0.0039
8)	2.000	-0.15	0.4202	0.0258			0.1027	0.0067	0.0374	0.0081	0.0596	0.0041
9)	2.000	-0.05	0.4074	0.0240			0.0893	0.0058	0.0369	0.0086	0.0642	0.0039
10)	2.000	0.05	0.4483	0.0188			0.1074	0.0048	0.1481	0.0146	0.0668	0.0031
11)	2.000	0.15	0.4882	0.0175			0.1214	0.0056	0.1439	0.0131	0.0712	0.0030
12)	2.000	0.25	0.5392	0.0175			0.1304	0.0054	0.1571	0.0145	0.0752	0.0030
13)	2.000	0.35	0.5712	0.0182			0.1198	0.0054	0.1597	0.0134	0.0844	0.0033
14)	2.000	0.45	0.5861	0.0176			0.1219	0.0047	0.1748	0.0137	0.0860	0.0032
15)	2.000	0.55	0.6110	0.0181			0.1124	0.0049	0.1537	0.0130	0.0936	0.0033
16)	2.000	0.65	0.5737	0.0187			0.1174	0.0044	0.1572	0.0140	0.1032	0.0036
17)	2.000	0.75	0.6170	0.0223			0.1082	0.0043	0.1302	0.0162	0.1121	0.0038
18)	2.000	0.84	0.6719	0.0342			0.1111	0.0077	0.0000	0.0000	0.1073	0.0055
19)	2.035	-0.85			0.0000	0.0000						
20)	2.035	-0.75			0.3818	0.1687						
21)	2.035	-0.65			0.0736	0.0253						
22)	2.035	-0.55			0.1091	0.0251						
23)	2.035	-0.45			0.1303	0.0350						
24)	2.035	-0.35			0.1177	0.0282						
25)	2.035	-0.25			0.0553	0.0127						
26)	2.035	-0.15			0.0786	0.0127						
27)	2.035	-0.05			0.1016	0.0148						
28)	2.035	0.05			0.0802	0.0120						
29)	2.035	0.15			0.0834	0.0121						
30)	2.035	0.25			0.1078	0.0140						
31)	2.035	0.35			0.1296	0.0164						
32)	2.035	0.45			0.1583	0.0180						
33)	2.035	0.55			0.1054	0.0145						
34)	2.035	0.65			0.1694	0.0209						
35)	2.035	0.75			0.1316	0.0299						
36)	2.035	0.84			0.0000	0.0000						
37)	2.100	-0.85	0.0000	0.0000	0.0000	0.0000	0.0000	0.0000	0.0000	0.0000	0.0000	0.0000
38)	2.100	-0.75	0.0000	0.0000	0.1347	0.0536	0.0927	0.0121	0.0000	0.0000	0.0117	0.0042
39)	2.100	-0.65	0.1585	0.0357	0.1150	0.0168	0.0926	0.0071	0.0000	0.0000	0.0152	0.0028
40)	2.100	-0.55	0.1757	0.0245	0.1086	0.0150	0.0934	0.0069	0.0000	0.0000	0.0219	0.0027
41)	2.100	-0.45	0.2133	0.0214	0.0982	0.0139	0.0993	0.0062	0.0207	0.0070	0.0301	0.0027
42)	2.100	-0.35	0.2733	0.0200	0.1287	0.0418	0.0936	0.0064	0.0460	0.0083	0.0345	0.0028
43)	2.100	-0.25	0.3303	0.0194	0.1782	0.0552	0.1102	0.0063	0.0965	0.0150	0.0425	0.0031
44)	2.100	-0.15	0.3370	0.0185	0.1353	0.0274	0.1249	0.0068	0.1017	0.0107	0.0466	0.0030
45)	2.100	-0.05	0.3729	0.0216	0.1264	0.0193	0.1420	0.0074	0.1679	0.0181	0.0561	0.0035
46)	2.100	0.05	0.4288	0.0152	0.1742	0.0250	0.1510	0.0058	0.1558	0.0104	0.0597	0.0027
47)	2.100	0.15	0.4534	0.0147	0.1934	0.0213	0.1637	0.0056	0.1567	0.0106	0.0606	0.0025
48)	2.100	0.25	0.5092	0.0151	0.3059	0.0286	0.1752	0.0052	0.1832	0.0108	0.0695	0.0026
49)	2.100	0.35	0.5776	0.0150	0.3563	0.0293	0.1811	0.0057	0.1631	0.0104	0.0760	0.0026
50)	2.100	0.45	0.5759	0.0146	0.3760	0.0283	0.1843	0.0049	0.1916	0.0096	0.0894	0.0027
51)	2.100	0.55	0.6492	0.0161	0.4561	0.0313	0.1580	0.0045	0.1900	0.0102	0.1027	0.0029
52)	2.100	0.65	0.6577	0.0172	0.4245	0.0248	0.1371	0.0046	0.1858	0.0117	0.1231	0.0034
53)	2.100	0.75	0.6869	0.0198	0.6135	0.0396	0.1277	0.0046	0.2033	0.0143	0.1417	0.0043
54)	2.100	0.84	0.7114	0.0280	0.6366	0.0652	0.0919	0.0061	0.1778	0.0188	0.1459	0.0049
55)	2.200	-0.85	0.0000	0.0000	0.0000	0.0000	0.0000	0.0000	0.0000	0.0000	0.0090	0.0045
56)	2.200	-0.75	0.0000	0.0000	0.2219	0.0236	0.0766	0.0086	0.0000	0.0000	0.0166	0.0031
57)	2.200	-0.65	0.0802	0.0246	0.1840	0.0162	0.0648	0.0066	0.0000	0.0000	0.0164	0.0027
58)	2.200	-0.55	0.1080	0.0169	0.1402	0.0139	0.0426	0.0057	0.0092	0.0056	0.0103	0.0020
59)	2.200	-0.45	0.1225	0.0145	0.1566	0.0447	0.0319	0.0045	0.0187	0.0080	0.0137	0.0021
60)	2.200	-0.35	0.1582	0.0133	0.1707	0.0433	0.0274	0.0047	0.0501	0.0117	0.0237	0.0024
61)	2.200	-0.25	0.1660	0.0128	0.0894	0.0264	0.0195	0.0042	0.0490	0.0097	0.0210	0.0024

<div align="center">TABLE III – continued</div>

Index	W (GeV)	$\cos\theta_{K^+}^{\mathrm{c.m.}}$	$\Sigma^0(1385)$		$\Lambda(1520)$		$\Lambda(1405)\to\Sigma^+\pi^-$		$\Lambda(1405)\to\Sigma^0\pi^0$		$\Lambda(1405)\to\Sigma^-\pi^+$	
			$d\sigma/d\cos\theta_{K^+}^{\mathrm{c.m.}}$	$\pm$	$d\sigma/d\cos\theta_{K^+}^{\mathrm{c.m.}}$	$\pm$	$d\sigma/d\cos\theta_{K^+}^{\mathrm{c.m.}}$	$\pm$	$d\sigma/d\cos\theta_{K^+}^{\mathrm{c.m.}}$	$\pm$	$d\sigma/d\cos\theta_{K^+}^{\mathrm{c.m.}}$	$\pm$
62)	2.200	-0.15	0.1873	0.0118	0.2019	0.0410	0.0220	0.0036	0.0488	0.0117	0.0238	0.0024
63)	2.200	-0.05	0.1936	0.0134	0.2077	0.0263	0.0349	0.0046	0.0622	0.0103	0.0294	0.0027
64)	2.200	0.05	0.2185	0.0097	0.2698	0.0257	0.0456	0.0042	0.0842	0.0079	0.0346	0.0020
65)	2.200	0.15	0.2817	0.0102	0.2544	0.0227	0.0620	0.0039	0.0710	0.0077	0.0334	0.0020
66)	2.200	0.25	0.3265	0.0108	0.3722	0.0256	0.0889	0.0047	0.0999	0.0070	0.0386	0.0021
67)	2.200	0.35	0.3327	0.0102	0.3629	0.0223	0.1037	0.0043	0.0763	0.0067	0.0527	0.0022
68)	2.200	0.45	0.3703	0.0101	0.5110	0.0256	0.1104	0.0040	0.1168	0.0070	0.0678	0.0024
69)	2.200	0.55	0.4328	0.0116	0.5309	0.0245	0.1116	0.0046	0.1201	0.0073	0.0846	0.0026
70)	2.200	0.65	0.4921	0.0131	0.6959	0.0308	0.1133	0.0043	0.1327	0.0079	0.1020	0.0030
71)	2.200	0.75	0.4580	0.0143	0.7051	0.0350	0.1085	0.0048	0.1531	0.0098	0.1106	0.0034
72)	2.200	0.84	0.5509	0.0202	0.6578	0.0532	0.0810	0.0049	0.1886	0.0142	0.1234	0.0047
73)	2.300	-0.85	0.0000	0.0000	0.2232	0.0584	0.0396	0.0088	0.0000	0.0000	0.0289	0.0070
74)	2.300	-0.75	0.0000	0.0000	0.1442	0.0169	0.0335	0.0066	0.0000	0.0000	0.0299	0.0032
75)	2.300	-0.65	0.1029	0.0254	0.1310	0.0148	0.0203	0.0038	0.0000	0.0000	0.0195	0.0027
76)	2.300	-0.55	0.1300	0.0173	0.1458	0.0123	0.0267	0.0032	0.0244	0.0097	0.0124	0.0020
77)	2.300	-0.45	0.0861	0.0114	0.1244	0.0112	0.0187	0.0026	0.0167	0.0090	0.0150	0.0018
78)	2.300	-0.35	0.0971	0.0099	0.1252	0.0281	0.0175	0.0026	0.0170	0.0070	0.0187	0.0021
79)	2.300	-0.25	0.0768	0.0091	0.1405	0.0212	0.0086	0.0019	0.0188	0.0069	0.0212	0.0020
80)	2.300	-0.15	0.0959	0.0081	0.1818	0.0283	0.0264	0.0026	0.0245	0.0065	0.0206	0.0020
81)	2.300	-0.05	0.1108	0.0087	0.1836	0.0192	0.0129	0.0021	0.0229	0.0060	0.0201	0.0019
82)	2.300	0.05	0.1394	0.0071	0.2169	0.0195	0.0273	0.0021	0.0215	0.0044	0.0214	0.0016
83)	2.300	0.15	0.1632	0.0072	0.2596	0.0197	0.0424	0.0024	0.0351	0.0047	0.0274	0.0017
84)	2.300	0.25	0.1958	0.0074	0.3080	0.0198	0.0507	0.0026	0.0438	0.0051	0.0396	0.0019
85)	2.300	0.35	0.2373	0.0073	0.3974	0.0197	0.0632	0.0026	0.0519	0.0048	0.0513	0.0019
86)	2.300	0.45	0.2652	0.0078	0.4039	0.0194	0.0699	0.0039	0.0592	0.0050	0.0708	0.0022
87)	2.300	0.55	0.3007	0.0086	0.5180	0.0229	0.0841	0.0039	0.0814	0.0062	0.0927	0.0025
88)	2.300	0.65	0.3534	0.0103	0.5526	0.0240	0.0953	0.0051	0.1353	0.0073	0.1184	0.0030
89)	2.300	0.75	0.4469	0.0123	0.5873	0.0288	0.0779	0.0050	0.1637	0.0081	0.1241	0.0032
90)	2.300	0.84	0.5282	0.0174	0.6168	0.0374	0.0723	0.0069	0.1685	0.0123	0.1306	0.0043
91)	2.400	-0.85	0.0000	0.0000	0.1033	0.0241	0.0179	0.0055	0.0000	0.0000	0.0350	0.0054
92)	2.400	-0.75	0.0000	0.0000	0.0830	0.0144	0.0222	0.0053	0.0000	0.0000	0.0362	0.0033
93)	2.400	-0.65	0.0591	0.0231	0.1001	0.0122	0.0092	0.0028	0.0000	0.0000	0.0282	0.0028
94)	2.400	-0.55	0.0785	0.0135	0.1486	0.0610	0.0185	0.0033	0.0255	0.0098	0.0194	0.0021
95)	2.400	-0.45	0.0514	0.0091	0.1126	0.0429	0.0075	0.0018	0.0200	0.0079	0.0140	0.0017
96)	2.400	-0.35	0.0609	0.0083	0.1135	0.0288	0.0121	0.0019	0.0191	0.0070	0.0182	0.0018
97)	2.400	-0.25	0.0530	0.0066	0.1002	0.0208	0.0073	0.0016	0.0127	0.0050	0.0134	0.0017
98)	2.400	-0.15	0.0625	0.0071	0.1194	0.0263	0.0117	0.0019	0.0168	0.0063	0.0055	0.0016
99)	2.400	-0.05	0.0669	0.0059	0.1538	0.0177	0.0118	0.0018	0.0178	0.0042	0.0115	0.0013
100)	2.400	0.05	0.0907	0.0054	0.1674	0.0161	0.0148	0.0015	0.0153	0.0032	0.0134	0.0014
101)	2.400	0.15	0.1088	0.0059	0.1796	0.0170	0.0296	0.0018	0.0221	0.0040	0.0176	0.0015
102)	2.400	0.25	0.1180	0.0055	0.2611	0.0164	0.0327	0.0020	0.0353	0.0040	0.0296	0.0016
103)	2.400	0.35	0.1453	0.0055	0.3293	0.0174	0.0414	0.0020	0.0446	0.0040	0.0409	0.0018
104)	2.400	0.45	0.1661	0.0061	0.3724	0.0178	0.0642	0.0023	0.0533	0.0047	0.0627	0.0020
105)	2.400	0.55	0.2275	0.0073	0.4989	0.0225	0.0726	0.0030	0.0815	0.0052	0.0855	0.0024
106)	2.400	0.65	0.2746	0.0090	0.5422	0.0256	0.0905	0.0036	0.0822	0.0064	0.1065	0.0029
107)	2.400	0.75	0.3637	0.0108	0.6443	0.0300	0.1096	0.0043	0.1486	0.0075	0.1301	0.0033
108)	2.400	0.84	0.5110	0.0160	0.6536	0.0389	0.0994	0.0062	0.1660	0.0106	0.1305	0.0043
109)	2.500	-0.85	0.0000	0.0000	0.0639	0.0227	0.0197	0.0054	0.0000	0.0000	0.0303	0.0046
110)	2.500	-0.75	0.0000	0.0000	0.0685	0.0126	0.0152	0.0035	0.0000	0.0000	0.0222	0.0028
111)	2.500	-0.65	0.0638	0.0250	0.0656	0.0099	0.0121	0.0024	0.0000	0.0000	0.0193	0.0022
112)	2.500	-0.55	0.0329	0.0094	0.0736	0.0088	0.0127	0.0023	0.0106	0.0087	0.0146	0.0017
113)	2.500	-0.45	0.0322	0.0064	0.0625	0.0072	0.0083	0.0013	0.0156	0.0061	0.0103	0.0014
114)	2.500	-0.35	0.0305	0.0063	0.0833	0.0282	0.0131	0.0018	0.0092	0.0055	0.0087	0.0014
115)	2.500	-0.25	0.0264	0.0045	0.0516	0.0068	0.0067	0.0011	0.0048	0.0024	0.0067	0.0012
116)	2.500	-0.15	0.0181	0.0047	0.0719	0.0196	0.0059	0.0012	0.0082	0.0035	0.0097	0.0014
117)	2.500	-0.05	0.0357	0.0038	0.0707	0.0101	0.0061	0.0010	0.0100	0.0028	0.0054	0.0009
118)	2.500	0.05	0.0481	0.0038	0.1340	0.0132	0.0082	0.0010	0.0085	0.0021	0.0050	0.0009
119)	2.500	0.15	0.0658	0.0041	0.1291	0.0108	0.0102	0.0010	0.0151	0.0026	0.0087	0.0010
120)	2.500	0.25	0.0821	0.0039	0.2324	0.0130	0.0176	0.0011	0.0199	0.0027	0.0132	0.0011
121)	2.500	0.35	0.0949	0.0042	0.2539	0.0124	0.0230	0.0013	0.0277	0.0029	0.0244	0.0013
122)	2.500	0.45	0.1190	0.0046	0.3256	0.0145	0.0392	0.0016	0.0303	0.0031	0.0421	0.0016
123)	2.500	0.55	0.1570	0.0057	0.3979	0.0177	0.0529	0.0021	0.0592	0.0041	0.0622	0.0020
124)	2.500	0.65	0.2177	0.0071	0.4366	0.0193	0.0765	0.0025	0.0719	0.0048	0.0808	0.0024
125)	2.500	0.75	0.3179	0.0092	0.5848	0.0255	0.0913	0.0030	0.1058	0.0060	0.1009	0.0028
126)	2.500	0.84	0.4095	0.0137	0.5648	0.0314	0.1048	0.0049	0.1361	0.0096	0.1110	0.0039
127)	2.600	-0.85	0.0000	0.0000	0.0573	0.0150	0.0060	0.0028	0.0000	0.0000	0.0232	0.0044
128)	2.600	-0.75	0.0000	0.0000	0.0521	0.0109	0.0129	0.0030	0.0000	0.0000	0.0194	0.0023
129)	2.600	-0.65	0.0832	0.0299	0.0461	0.0078	0.0068	0.0017	0.0000	0.0000	0.0113	0.0017
130)	2.600	-0.55	0.0435	0.0102	0.0428	0.0069	0.0100	0.0017	0.0112	0.0079	0.0056	0.0012

TABLE III – continued

Index	W (GeV)	$\cos\theta_{K^+}^{\text{c.m.}}$	$\Sigma^0(1385)$ $d\sigma/d\cos\theta_{K^+}^{\text{c.m.}}$	$\pm$	$\Lambda(1520)$ $d\sigma/d\cos\theta_{K^+}^{\text{c.m.}}$	$\pm$	$\Lambda(1405)\to\Sigma^+\pi^-$ $d\sigma/d\cos\theta_{K^+}^{\text{c.m.}}$	$\pm$	$\Lambda(1405)\to\Sigma^0\pi^0$ $d\sigma/d\cos\theta_{K^+}^{\text{c.m.}}$	$\pm$	$\Lambda(1405)\to\Sigma^-\pi^+$ $d\sigma/d\cos\theta_{K^+}^{\text{c.m.}}$	$\pm$
131)	2.600	-0.45	0.0280	0.0065	0.0270	0.0056	0.0090	0.0013	0.0043	0.0038	0.0084	0.0011
132)	2.600	-0.35	0.0197	0.0045	0.0214	0.0063	0.0083	0.0013	0.0075	0.0029	0.0072	0.0011
133)	2.600	-0.25	0.0178	0.0035	0.0306	0.0051	0.0080	0.0010	0.0056	0.0026	0.0052	0.0010
134)	2.600	-0.15	0.0081	0.0032	0.0276	0.0047	0.0046	0.0008	0.0046	0.0025	0.0079	0.0010
135)	2.600	-0.05	0.0185	0.0027	0.0437	0.0090	0.0044	0.0006	0.0114	0.0026	0.0013	0.0006
136)	2.600	0.05	0.0314	0.0028	0.0539	0.0070	0.0036	0.0007	0.0041	0.0014	0.0027	0.0006
137)	2.600	0.15	0.0444	0.0028	0.0867	0.0080	0.0055	0.0007	0.0058	0.0016	0.0022	0.0006
138)	2.600	0.25	0.0481	0.0028	0.1252	0.0080	0.0099	0.0008	0.0125	0.0017	0.0060	0.0007
139)	2.600	0.35	0.0548	0.0030	0.1944	0.0100	0.0112	0.0008	0.0181	0.0021	0.0125	0.0009
140)	2.600	0.45	0.0706	0.0034	0.2559	0.0115	0.0255	0.0012	0.0298	0.0024	0.0247	0.0012
141)	2.600	0.55	0.1106	0.0046	0.3306	0.0159	0.0427	0.0016	0.0340	0.0031	0.0412	0.0016
142)	2.600	0.65	0.1580	0.0055	0.3906	0.0178	0.0649	0.0020	0.0555	0.0039	0.0606	0.0019
143)	2.600	0.75	0.2498	0.0078	0.5053	0.0214	0.0922	0.0029	0.0903	0.0052	0.0773	0.0024
144)	2.600	0.84	0.3048	0.0118	0.6184	0.0341	0.0982	0.0040	0.1164	0.0081	0.0924	0.0035
145)	2.700	-0.85	0.0000	0.0000	0.0362	0.0213	0.0093	0.0043	0.0000	0.0000	0.0151	0.0041
146)	2.700	-0.75	0.0000	0.0000	0.0551	0.0120	0.0074	0.0024	0.0000	0.0000	0.0120	0.0021
147)	2.700	-0.65	0.1310	0.0433	0.0329	0.0066	0.0059	0.0016	0.0000	0.0000	0.0041	0.0012
148)	2.700	-0.55	0.0336	0.0106	0.0243	0.0061	0.0066	0.0014	0.0117	0.0068	0.0045	0.0011
149)	2.700	-0.45	0.0220	0.0073	0.0293	0.0054	0.0063	0.0010	0.0061	0.0040	0.0046	0.0009
150)	2.700	-0.35	0.0107	0.0042	0.0214	0.0046	0.0068	0.0010	0.0057	0.0038	0.0041	0.0008
151)	2.700	-0.25	0.0098	0.0038	0.0248	0.0054	0.0070	0.0014	0.0027	0.0026	0.0037	0.0008
152)	2.700	-0.15	0.0089	0.0026	0.0181	0.0036	0.0030	0.0006	0.0032	0.0018	0.0032	0.0006
153)	2.700	-0.05	0.0138	0.0022	0.0281	0.0035	0.0030	0.0005	0.0015	0.0013	0.0023	0.0005
154)	2.700	0.05	0.0170	0.0022	0.0498	0.0093	0.0043	0.0006	0.0040	0.0015	0.0018	0.0005
155)	2.700	0.15	0.0216	0.0021	0.0496	0.0061	0.0038	0.0006	0.0036	0.0012	0.0013	0.0004
156)	2.700	0.25	0.0233	0.0021	0.0908	0.0078	0.0056	0.0006	0.0042	0.0012	0.0027	0.0005
157)	2.700	0.35	0.0352	0.0024	0.1365	0.0092	0.0057	0.0007	0.0124	0.0017	0.0068	0.0007
158)	2.700	0.45	0.0516	0.0030	0.1467	0.0098	0.0147	0.0010	0.0154	0.0021	0.0118	0.0010
159)	2.700	0.55	0.0802	0.0040	0.2389	0.0135	0.0287	0.0014	0.0310	0.0027	0.0258	0.0014
160)	2.700	0.65	0.1194	0.0050	0.3309	0.0168	0.0480	0.0018	0.0466	0.0033	0.0413	0.0017
161)	2.700	0.75	0.1963	0.0072	0.4330	0.0202	0.0720	0.0026	0.0862	0.0051	0.0661	0.0024
162)	2.700	0.83	0.2617	0.0124	0.4765	0.0317	0.0851	0.0048	0.1070	0.0083	0.0785	0.0040
163)	2.800	-0.85	0.0000	0.0000	0.0000	0.0000	0.0036	0.0020	0.0000	0.0000	0.0227	0.0051
164)	2.800	-0.75	0.0000	0.0000	0.0400	0.0163	0.0113	0.0028	0.0000	0.0000	0.0077	0.0022
165)	2.800	-0.65	0.1617	0.1126	0.0320	0.0071	0.0061	0.0021	0.0000	0.0000	0.0052	0.0014
166)	2.800	-0.55	0.0289	0.0160	0.0143	0.0049	0.0052	0.0011	0.0000	0.0000	0.0025	0.0008
167)	2.800	-0.45	0.0172	0.0081	0.0163	0.0046	0.0072	0.0013	0.0044	0.0046	0.0018	0.0006
168)	2.800	-0.35	0.0100	0.0055	0.0177	0.0039	0.0042	0.0009	0.0009	0.0028	0.0019	0.0006
169)	2.800	-0.25	0.0160	0.0059	0.0137	0.0058	0.0035	0.0008	0.0013	0.0021	0.0022	0.0007
170)	2.800	-0.15	0.0069	0.0023	0.0221	0.0036	0.0023	0.0005	0.0034	0.0018	0.0029	0.0005
171)	2.800	-0.05	0.0092	0.0019	0.0264	0.0033	0.0026	0.0006	0.0040	0.0014	0.0021	0.0004
172)	2.800	0.05	0.0108	0.0019	0.0348	0.0072	0.0019	0.0004	0.0033	0.0013	0.0014	0.0004
173)	2.800	0.15	0.0108	0.0017	0.0441	0.0036	0.0032	0.0004	0.0035	0.0012	0.0019	0.0004
174)	2.800	0.25	0.0100	0.0015	0.0429	0.0057	0.0042	0.0005	0.0026	0.0011	0.0016	0.0004
175)	2.800	0.35	0.0261	0.0021	0.0786	0.0076	0.0044	0.0006	0.0075	0.0013	0.0034	0.0006
176)	2.800	0.45	0.0357	0.0028	0.1259	0.0098	0.0092	0.0008	0.0104	0.0019	0.0093	0.0009
177)	2.800	0.55	0.0694	0.0037	0.1690	0.0113	0.0190	0.0012	0.0195	0.0025	0.0201	0.0013
178)	2.800	0.65	0.1050	0.0048	0.2986	0.0153	0.0376	0.0017	0.0409	0.0033	0.0367	0.0018
179)	2.800	0.75	0.1832	0.0074	0.4212	0.0209	0.0724	0.0028	0.0645	0.0048	0.0574	0.0026
180)	2.800	0.83	0.2172	0.0118	0.4534	0.0323	0.0862	0.0050	0.1155	0.0088	0.0770	0.0045